

# Enhanced Cycling Stability in the Anion Redox Material P3-Type Zn-Substituted Sodium Manganese Oxide

Stephanie F. Linnell,<sup>[a, b]</sup> Moritz Hirsbrunner,<sup>[c]</sup> Saki Imada,<sup>[d]</sup> Giannantonio Cibin,<sup>[e]</sup> Aaron B. Naden,<sup>[a]</sup> Alan V. Chadwick,<sup>[f]</sup> John T. S. Irvine,<sup>[a, b]</sup> Laurent C. Duda,<sup>[c]</sup> and A. Robert Armstrong<sup>\*[a, b]</sup>

Sodium layered oxides showing oxygen redox activity are promising positive electrodes for sodium-ion batteries (SIBs). However, structural degradation typically results in limited reversibility of the oxygen redox activity. Herein, the effect of Zn-doping on the electrochemical properties of P3-type sodium manganese oxide, synthesised under air and oxygen is investigated for the first time. Air-Na<sub>0.67</sub>Mn<sub>0.9</sub>Zn<sub>0.1</sub>O<sub>2</sub> and Oxy-Na<sub>0.67</sub>Mn<sub>0.9</sub>Zn<sub>0.1</sub>O<sub>2</sub> exhibit stable cycling performance between 1.8 and 3.8 V, each maintaining 96% of their initial capacity

after 30 cycles, where Mn<sup>3+</sup>/Mn<sup>4+</sup> redox dominates. Increasing the voltage range to 1.8–4.3 V activates oxygen redox. For the material synthesised under air, oxygen redox activity is based on Zn, with limited reversibility. The additional transition metal vacancies in the material synthesised under oxygen result in enhanced oxygen redox reversibility with small voltage hysteresis. These results may assist the development of high-capacity and structurally stable oxygen redox-based materials for SIBs.

## 1. Introduction

The efficient use of renewable energy sources such as wind and solar is crucial for a sustainable future. However, these are intermittent and may be localized geographically, and therefore, energy storage systems are required to allow for the storage and release of energy when the supply is not matched by the demand.<sup>[1]</sup> Rechargeable batteries are considered a promising solution, providing they can deliver an efficient, cost-

effective, and sustainable storage strategy on a large-scale. In this respect, SIBs are promising candidates, owing to the low cost and abundance of sodium and ability to store and transport SIBs at 0 V.<sup>[2–4]</sup>

Layered sodium transition metal oxides, Na<sub>x</sub>M<sub>y</sub>O<sub>2</sub> (0.4 ≤ x ≤ 1.0, and M = transition metal ion(s)) have become the positive electrode materials of choice for SIBs. These layered oxides can adopt the O3, P2 and P3 polymorphs, in which the Na<sup>+</sup> ions can be accommodated in either octahedral (O) or trigonal prismatic (P) sites and the number describes the number of MO<sub>2</sub> layers in the unit cell.<sup>[5]</sup> These materials tend to exhibit structural transformations at high voltages, between the P-type and O-type phases, induced by gliding of the MO<sub>2</sub> layers upon insertion/extraction of Na<sup>+</sup> ions and, in the case of Mn-based materials, because of the presence of Jahn-Teller active Mn<sup>3+</sup> ions. These distortions lead to large unit cell volume changes and lattice strain, which is detrimental to the cycling performance.<sup>[6]</sup> The possibility of obtaining additional capacity in Mn-based materials originating from oxygen redox chemistry has attracted considerable attention.<sup>[4,7]</sup> For example Na<sub>4/7</sub>[□<sub>1/7</sub> Mn<sub>6/7</sub>]O<sub>2</sub> (where □ represents a transition metal vacancy), contains Mn vacancies and therefore O 2p nonbonding orbitals which enable reversible oxygen redox.<sup>[7]</sup> Upon cycling Na<sub>4/7</sub>[□<sub>1/7</sub> Mn<sub>6/7</sub>]O<sub>2</sub>, its layered structure and P3-type oxygen stacking sequence (ABBCCA) are maintained.<sup>[8,9]</sup> Consequently, Na<sub>4/7</sub>[□<sub>1/7</sub> Mn<sub>6/7</sub>]O<sub>2</sub> shows more reversible oxygen redox compared with other sodium-based oxygen redox active materials with negligible voltage hysteresis and can deliver a specific capacity of up to ~200 mAh g<sup>-1</sup>.<sup>[7,10,11]</sup> However, Na<sub>4/7</sub>[□<sub>1/7</sub> Mn<sub>6/7</sub>]O<sub>2</sub> shows a capacity retention of ~63% over 60 cycles when both cation and anion redox reactions are used.<sup>[7,11]</sup> Therefore, to enhance the long-term cyclability of these materials over the high voltage regions, several different approaches have been adopted to improve the structural integrity. Substitution of Mn by electrochemically active elements, like Ni<sup>2+</sup>, Fe<sup>3+</sup> or Co<sup>3+</sup>,

[a] Dr. S. F. Linnell, Dr. A. B. Naden, Prof. J. T. S. Irvine, Dr. A. R. Armstrong  
School of Chemistry  
University of St Andrews  
St Andrews, Fife, KY16 9ST, United Kingdom  
E-mail: ara@st-andrews.ac.uk


[b] Dr. S. F. Linnell, Prof. J. T. S. Irvine, Dr. A. R. Armstrong  
The Faraday Institution  
Quad One, Harwell Science and Innovation Campus, Didcot, OX11 0RA,  
United Kingdom


[c] M. Hirsbrunner, Dr. L. C. Duda  
Department of Physics and Astronomy, Division of Molecular and  
Condensed Matter Physics  
Uppsala University  
Uppsala, S-75120, Sweden

[d] Prof. S. Imada  
Faculty of Electrical Engineering and Electronics  
Kyoto Institute of Technology  
Sakyo, Kyoto 606-8585, Japan

[e] Dr. G. Cibin  
Diamond Light Source Ltd  
Diamond House Harwell Science & Innovation Campus, Didcot, Oxfordshire,  
OX11 0DE, United Kingdom

[f] Prof. A. V. Chadwick  
School of Physical Sciences  
University of Kent  
Canterbury, Kent, CT2 7NH, United Kingdom

 Supporting information for this article is available on the WWW under <https://doi.org/10.1002/celec.202200240>

 © 2022 The Authors. ChemElectroChem published by Wiley-VCH GmbH. This is an open access article under the terms of the Creative Commons Attribution License, which permits use, distribution and reproduction in any medium, provided the original work is properly cited.

facilitates the electron transfer between the O 2p states and transition metal 3d bands, typically *via* a reductive coupling mechanism, thereby stabilizing the oxygen redox activity.<sup>[12–15]</sup> Doping with electrochemically inactive elements, Li<sup>+</sup>, Mg<sup>2+</sup>, and Zn<sup>2+</sup>, forms ionic Li–O, Mg–O and Zn–O bonds, such that the electrons in these bonds are localized on the oxygen anions, creating O 2p nonbonding orbitals which participate in the charge compensation mechanism.<sup>[16–21]</sup>

A previous study reported the substitution of Mn<sup>3+</sup> ions by Mg<sup>2+</sup> ions to stabilize the P3-type structure.<sup>[22]</sup> P3-Na<sub>0.67</sub>Mn<sub>0.8</sub>Mg<sub>0.2</sub>O<sub>2</sub> synthesised under air and quenched, exhibited an oxygen redox process on charge at 4.15 V with large voltage hysteresis, whereas when synthesised under oxygen and slow cooled, the material contained 4% vacancies and exhibited enhanced oxygen redox reversibility at 4.2 V. The transition metal vacancies in Oxy-Na<sub>0.67</sub>Mn<sub>0.8</sub>Mg<sub>0.2</sub>O<sub>2</sub>, enabled unpaired O 2p orbitals independent of the substituted Mg to form, which stabilized the P3 structure upon Na<sup>+</sup> ion extraction and reduced the structural transformation to the O'3 structure upon Na<sup>+</sup> ion insertion.<sup>[22]</sup>

Substitution using more electronegative Zn<sup>2+</sup> ions (Pauling electronegativity values: Zn 1.65 and Mg 1.31, respectively) has also been used to suppress the Jahn-Teller distortion by diluting the Mn<sup>3+</sup> ions. Doping with Zn<sup>2+</sup> ions stabilized the structure of P2-Na<sub>0.67</sub>Mn<sub>0.6</sub>Fe<sub>0.3</sub>Zn<sub>0.1</sub>O<sub>2</sub> upon cycling, resulting in superior electrochemical properties when compared with those of the undoped P2-Na<sub>0.67</sub>Mn<sub>0.6</sub>Fe<sub>0.4</sub>O<sub>2</sub> material.<sup>[23]</sup> Similarly, Yang and co-workers have explored a series of Zn-doped P2-Na<sub>0.66</sub>Ni<sub>0.33-x</sub>Zn<sub>x</sub>Mn<sub>0.67</sub>O<sub>2</sub> ( $x=0, 0.07, 0.14$ ) materials that exhibit improved electrochemical performance, smoother voltage profiles and reduced structural transformation from the P2 to P'2 structure, compared with P2-Na<sub>0.66</sub>Ni<sub>0.33</sub>Mn<sub>0.67</sub>O<sub>2</sub>.<sup>[24,25]</sup> Bai *et al.* studied the effects of Zn doping in P2-Na<sub>2/3</sub>Mn<sub>7/9</sub>Zn<sub>2/9</sub>O<sub>2</sub>. This phase behaved in an analogous manner to the Mg-substituted P2-Na<sub>0.67</sub>Mg<sub>0.28</sub>Mn<sub>0.72</sub>O<sub>2</sub> material,<sup>[26]</sup> as well as showing the participation of oxygen anions in the charge compensation mechanism without the release of O<sub>2</sub>.<sup>[20]</sup> Despite their similarities, Na<sub>2/3</sub>Mn<sub>7/9</sub>Zn<sub>2/9</sub>O<sub>2</sub> revealed cation migration, leading to poor cycling performance and density functional theory (DFT) calculations demonstrated that the oxygen redox activity originates from the presence of a nonbonding O 2p state.<sup>[20]</sup>

Driven by the efficiency of doping with Zn in stabilizing the structures of P2-type materials, we have studied the effects of Zn-doping on P3-type Na<sub>0.67</sub>Mn<sub>0.9</sub>Zn<sub>0.1</sub>O<sub>2</sub>, in both the absence and presence of transition metal vacancies. Na<sub>0.67</sub>Mn<sub>0.9</sub>Zn<sub>0.1</sub>O<sub>2</sub>, synthesised under air and quenched, contains very few transition metal vacancies, and exhibits oxygen redox with significant voltage hysteresis. By contrast, Na<sub>0.67</sub>Mn<sub>0.9</sub>Zn<sub>0.1</sub>O<sub>2</sub>, synthesised under oxygen and slow cooled, contains 6% vacancies and shows enhanced oxygen redox reversibility, demonstrating the advantages of vacancies. Structural analysis indicates that the good cycling performance is due to the stable framework structure of P3-Na<sub>0.67</sub>Mn<sub>0.9</sub>Zn<sub>0.1</sub>O<sub>2</sub>.

## 2. Results and Discussion

### 2.1. Characterization of Air-Na<sub>0.67</sub>Mn<sub>0.9</sub>Zn<sub>0.1</sub>O<sub>2</sub> and Oxy-Na<sub>0.67</sub>Mn<sub>0.9</sub>Zn<sub>0.1</sub>O<sub>2</sub>

P3-type Na<sub>0.67</sub>Mn<sub>0.9</sub>Zn<sub>0.1</sub>O<sub>2</sub> are based on the P3 layered Na<sub>4/7</sub>[□<sub>1/7</sub>Mn<sub>6/7</sub>]O<sub>2</sub> material in which Mn ions are substituted by Zn ions.<sup>[7,27]</sup> The powder X-ray diffraction (PXRD) patterns of Air-Na<sub>0.67</sub>Mn<sub>0.9</sub>Zn<sub>0.1</sub>O<sub>2</sub> and Oxy-Na<sub>0.67</sub>Mn<sub>0.9</sub>Zn<sub>0.1</sub>O<sub>2</sub> can be fully indexed to an ideal P3 structure with the space group *R3m*, where Na<sup>+</sup> ions occupy trigonal prismatic sites, and Mn and Zn ions are in octahedral sites with ABCCA oxygen stacking, as illustrated in Figure S1. All diffraction peaks are well-fitted by Rietveld refinement using this model for Air-Na<sub>0.67</sub>Mn<sub>0.9</sub>Zn<sub>0.1</sub>O<sub>2</sub> and Oxy-Na<sub>0.67</sub>Mn<sub>0.9</sub>Zn<sub>0.1</sub>O<sub>2</sub> and the profile fits are shown in Figure 1(a, b), respectively. The refined structural parameters are presented in Table S1. These results show that the unit cell volume of Oxy-Na<sub>0.67</sub>Mn<sub>0.9</sub>Zn<sub>0.1</sub>O<sub>2</sub> (121.75(3) Å<sup>3</sup>) is smaller than that of Air-Na<sub>0.67</sub>Mn<sub>0.9</sub>Zn<sub>0.1</sub>O<sub>2</sub> (122.08(2) Å<sup>3</sup>), associated with a contraction in the *a* parameter. Since *a* is strongly correlated with the M–O bond length, this is consistent with a higher Mn oxidation state in Oxy-Na<sub>0.67</sub>Mn<sub>0.9</sub>Zn<sub>0.1</sub>O<sub>2</sub>. This could arise either because of variation in the Na content or the presence of transition metal vacancies. Since the refined Na occupancies (Table S1) for these materials are essentially the same, it is reasonable to assume that the contraction in *a* is due to vacancies on the Mn sites in Oxy-Na<sub>0.67</sub>Mn<sub>0.9</sub>Zn<sub>0.1</sub>O<sub>2</sub>. Synthesis of Na<sub>0.67</sub>Mn<sub>0.9</sub>Zn<sub>0.1</sub>O<sub>2</sub> under more oxidizing conditions results in the uptake of more oxygen, raising the average Mn oxidation state closer to Mn<sup>4+</sup> which generates vacancies on the Mn sites for charge compensation, as reported in a range of related systems.<sup>[5,18,24–28]</sup> The refined occupancies (Table S1) reveal that Oxy-Na<sub>0.67</sub>Mn<sub>0.9</sub>Zn<sub>0.1</sub>O<sub>2</sub> contains 6% vacancies, Na<sub>0.67</sub>Mn<sub>0.85</sub><sup>+3.71</sup>Zn<sub>0.09</sub>□<sub>0.06</sub>O<sub>2</sub> while Air-Na<sub>0.67</sub>Mn<sub>0.9</sub>Zn<sub>0.1</sub>O<sub>2</sub> contains very few transition metal vacancies, Na<sub>0.62</sub>Mn<sub>0.9</sub><sup>+3.53</sup>Zn<sub>0.1</sub>O<sub>2</sub>. However, it should be noted that that a small amount of vacancies could form at 625 °C in air despite quenching the material.<sup>[31]</sup>

As-synthesised Air-Na<sub>0.67</sub>Mn<sub>0.75</sub>Zn<sub>0.25</sub>O<sub>2</sub> was examined by powder neutron diffraction. A number of reflections are unindexed on the basis of the simple P3 model and can be indexed on the basis of a superlattice model (space group *Cm*), in which Zn<sup>2+</sup> ions are in the centre of a honeycomb arrangement surrounded by Mn ions (Figure S2). The profile fit and corresponding refined structural parameters are presented in Figure S2 and Table S2, respectively. Given the size difference between Mn<sup>4+</sup> (0.53 Å) and Zn<sup>2+</sup> (0.74 Å) ions,<sup>[32]</sup> it is expected that Air-Na<sub>0.67</sub>Mn<sub>0.9</sub>Zn<sub>0.1</sub>O<sub>2</sub> and Oxy-Na<sub>0.67</sub>Mn<sub>0.9</sub>Zn<sub>0.1</sub>O<sub>2</sub> will exhibit similar ordering behaviour. Weak superlattice reflections are discernible in the XRD patterns but there is insufficient contrast between Mn and Zn to permit refinement. Previous work has demonstrated the importance of honeycomb-type cation ordering on stable oxygen redox activity in Na<sub>2</sub>RuO<sub>3</sub>.<sup>[33]</sup>

The morphologies of Air-Na<sub>0.67</sub>Mn<sub>0.9</sub>Zn<sub>0.1</sub>O<sub>2</sub> and Oxy-Na<sub>0.67</sub>Mn<sub>0.9</sub>Zn<sub>0.1</sub>O<sub>2</sub> are shown in Figure 1(c) and (d), respectively, exhibiting agglomerated primary particles of around 100 nm in size. The SEM micrographs show that the different synthetic conditions did not have any discernible effect on the

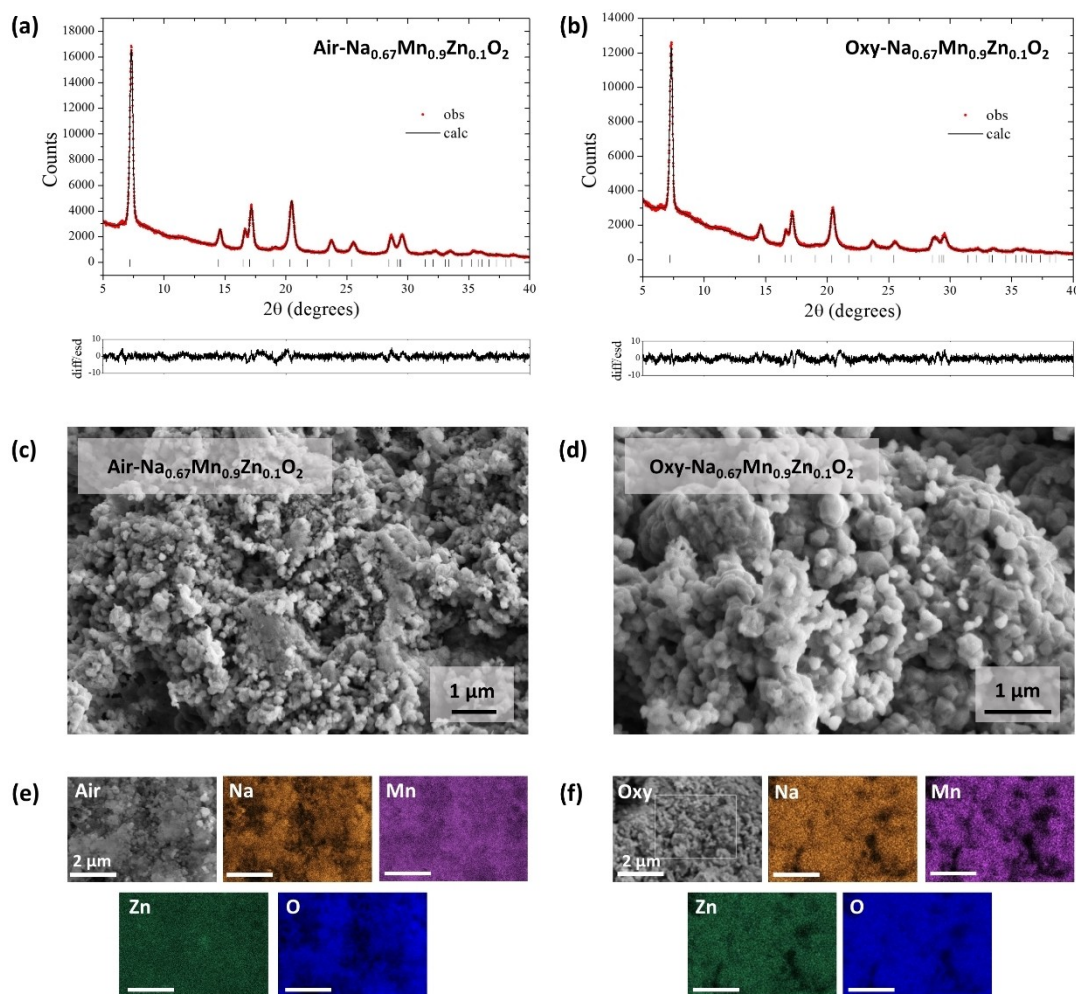


**Figure 1.** Laboratory X-ray Rietveld fit of as-synthesized (a)  $\text{Air-Na}_{0.67}\text{Mn}_{0.9}\text{Zn}_{0.1}\text{O}_2$  and (b)  $\text{Oxy-Na}_{0.67}\text{Mn}_{0.9}\text{Zn}_{0.1}\text{O}_2$ . Observed data points are shown in red, with fitted profile in black. Tick marks indicate allowed reflections for the P3 phase. SEM micrographs of as-synthesized (c)  $\text{Air-Na}_{0.67}\text{Mn}_{0.9}\text{Zn}_{0.1}\text{O}_2$  and (d)  $\text{Oxy-Na}_{0.67}\text{Mn}_{0.9}\text{Zn}_{0.1}\text{O}_2$ . EDS mapping of (e)  $\text{Air-Na}_{0.67}\text{Mn}_{0.9}\text{Zn}_{0.1}\text{O}_2$  and (f)  $\text{Oxy-Na}_{0.67}\text{Mn}_{0.9}\text{Zn}_{0.1}\text{O}_2$ .

morphologies. The EDS elemental maps for  $\text{Air-Na}_{0.67}\text{Mn}_{0.9}\text{Zn}_{0.1}\text{O}_2$  and  $\text{Oxy-Na}_{0.67}\text{Mn}_{0.9}\text{Zn}_{0.1}\text{O}_2$  are shown in Figure 1(e) and (f), respectively, and show uniform elemental distribution of sodium, manganese, zinc, and oxygen for both materials.

## 2.2. Electrochemical Properties

The electrochemical properties of  $\text{Air-Na}_{0.67}\text{Mn}_{0.9}\text{Zn}_{0.1}\text{O}_2$  and  $\text{Oxy-Na}_{0.67}\text{Mn}_{0.9}\text{Zn}_{0.1}\text{O}_2$  were explored. Half-cells of  $\text{Air-Na}_{0.67}\text{Mn}_{0.9}\text{Zn}_{0.1}\text{O}_2$  and  $\text{Oxy-Na}_{0.67}\text{Mn}_{0.9}\text{Zn}_{0.1}\text{O}_2$  were cycled in galvanostatic mode within the voltage ranges 1.8–3.8 V and 1.8–4.3 V, at rates of  $10 \text{ mA g}^{-1}$  and  $100 \text{ mA g}^{-1}$ . Figure 2(a) and (b) show the galvanostatic charge/discharge voltage profiles and the corresponding differential capacity plots, respectively, of  $\text{Air-Na}_{0.67}\text{Mn}_{0.9}\text{Zn}_{0.1}\text{O}_2$  and  $\text{Oxy-Na}_{0.67}\text{Mn}_{0.9}\text{Zn}_{0.1}\text{O}_2$  electrodes cycled between 1.8 and 3.8 V during the second cycle at a rate of  $10 \text{ mA g}^{-1}$ . Both materials show smooth load curves due to the dilution of the Jahn-Teller active  $\text{Mn}^{3+}$  ions by substitution

of  $\text{Zn}^{2+}$  ions.<sup>[22,34]</sup> Extended plateaus are observed at around 2.1 V for both materials, in keeping with the differential capacity plots which show oxidation and reduction peaks at 2.2 and 2.1 V, respectively, associated with the  $\text{Mn}^{4+}/\text{Mn}^{3+}$  redox couple.

Figure 2(e) shows the galvanostatic cycling performance of  $\text{Air-Na}_{0.67}\text{Mn}_{0.9}\text{Zn}_{0.1}\text{O}_2$  and  $\text{Oxy-Na}_{0.67}\text{Mn}_{0.9}\text{Zn}_{0.1}\text{O}_2$  electrodes cycled between 1.8 and 3.8 V at 10 and  $100 \text{ mA g}^{-1}$ .  $\text{Air-Na}_{0.67}\text{Mn}_{0.9}\text{Zn}_{0.1}\text{O}_2$  and  $\text{Oxy-Na}_{0.67}\text{Mn}_{0.9}\text{Zn}_{0.1}\text{O}_2$  exhibit excellent capacity retention at both rates. At the slower rate of  $10 \text{ mA g}^{-1}$ ,  $\text{Air-Na}_{0.67}\text{Mn}_{0.9}\text{Zn}_{0.1}\text{O}_2$  and  $\text{Oxy-Na}_{0.67}\text{Mn}_{0.9}\text{Zn}_{0.1}\text{O}_2$  have a capacity retention of 90% and 98% over 50 cycles, respectively. At the faster rate of  $100 \text{ mA g}^{-1}$ , the initial discharge capacity decreases from 167 to  $153 \text{ mA h g}^{-1}$  for  $\text{Air-Na}_{0.67}\text{Mn}_{0.9}\text{Zn}_{0.1}\text{O}_2$  and from 159 to  $144 \text{ mA h g}^{-1}$  for  $\text{Oxy-Na}_{0.67}\text{Mn}_{0.9}\text{Zn}_{0.1}\text{O}_2$  but show good capacity retention of 90% and 93% over 50 cycles. However, Figure 2(c) and (d) show that the polarization increases in the lower-voltage region (below 2.5 V) when  $\text{Air-Na}_{0.67}\text{Mn}_{0.9}\text{Zn}_{0.1}\text{O}_2$  and  $\text{Oxy-Na}_{0.67}\text{Mn}_{0.9}\text{Zn}_{0.1}\text{O}_2$  are cycled at  $100 \text{ mA g}^{-1}$ . This is within the region where a cooperative Jahn-

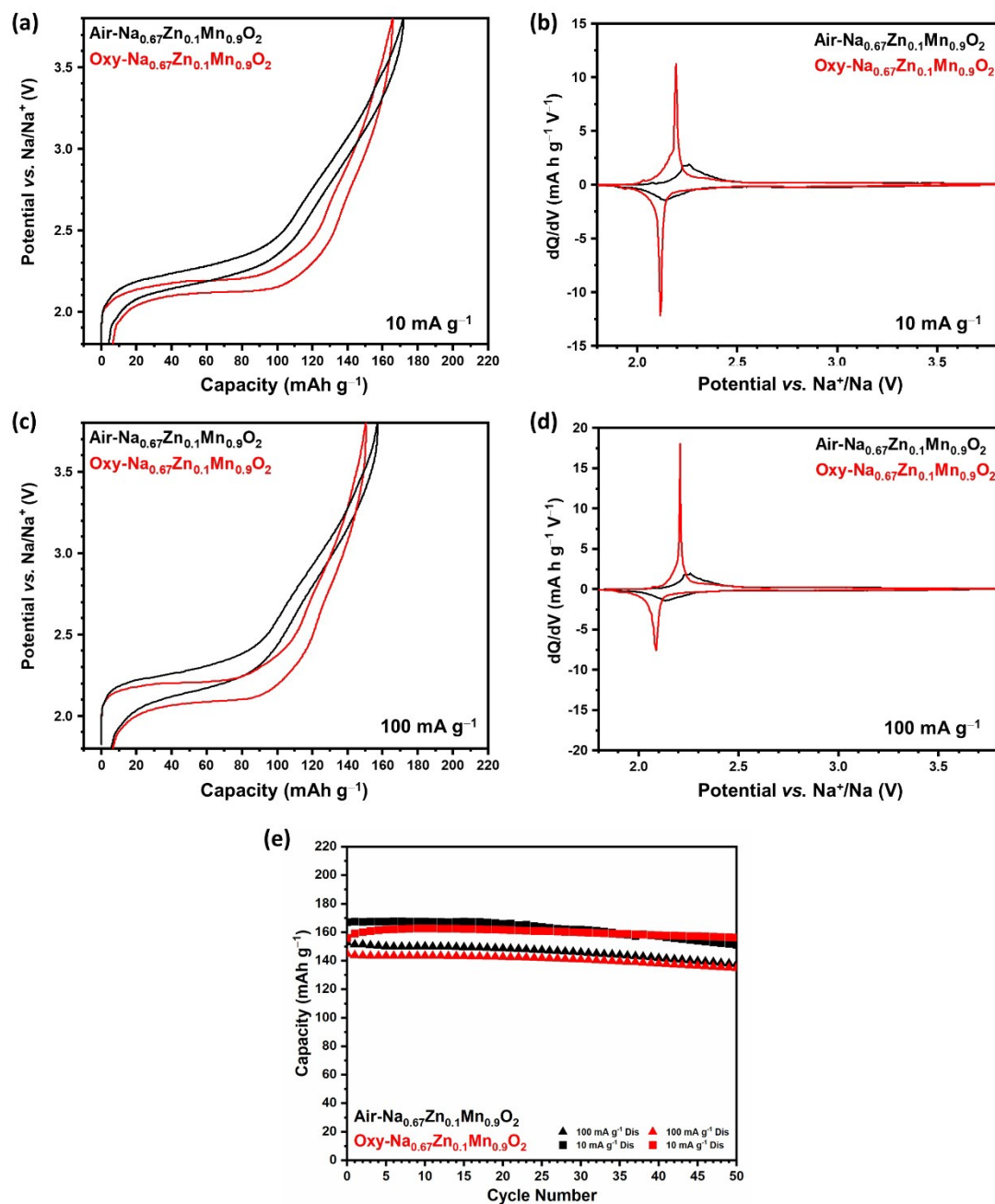


**Figure 2.** Charge/discharge curves of Air-Na<sub>0.67</sub>Mn<sub>0.9</sub>Zn<sub>0.1</sub>O<sub>2</sub> (black) and Oxy-Na<sub>0.67</sub>Mn<sub>0.9</sub>Zn<sub>0.1</sub>O<sub>2</sub> (red) half-cells cycled at 30 °C between 1.8–3.8 V, showing the second cycle at a rate of (a) 10 mA g<sup>-1</sup> and (c) 100 mA g<sup>-1</sup>. The differential capacity versus voltage plots of Air-Na<sub>0.67</sub>Mn<sub>0.9</sub>Zn<sub>0.1</sub>O<sub>2</sub> (black) and Oxy-Na<sub>0.67</sub>Mn<sub>0.9</sub>Zn<sub>0.1</sub>O<sub>2</sub> (red) half-cells, corresponding to the second cycle in the voltage range 1.8–3.8 V at a rate of (b) 10 mA g<sup>-1</sup> and (d) 100 mA g<sup>-1</sup>. (e) Galvanostatic cycling performance of Air-Na<sub>0.67</sub>Mn<sub>0.9</sub>Zn<sub>0.1</sub>O<sub>2</sub> (black) and Oxy-Na<sub>0.67</sub>Mn<sub>0.9</sub>Zn<sub>0.1</sub>O<sub>2</sub> (red), cycled between 1.8–3.8 V. Square-shaped symbols represent discharge capacities of cells cycled at a rate of 10 mA g<sup>-1</sup> and triangle-shaped symbols represent discharge capacities of cells cycled at a rate of 100 mA g<sup>-1</sup>.

Teller distortion is likely to occur with the intercalation of more Na<sup>+</sup> ions, as will be outlined below.

To investigate the oxygen redox process the upper voltage cut-off was extended to 4.3 V. The galvanostatic charge/discharge voltage profiles and corresponding differential capacity plots for Air-Na<sub>0.67</sub>Mn<sub>0.9</sub>Zn<sub>0.1</sub>O<sub>2</sub> and Oxy-Na<sub>0.67</sub>Mn<sub>0.9</sub>Zn<sub>0.1</sub>O<sub>2</sub> electrodes cycled over the larger voltage range of 1.8–4.3 V during the first cycle at a rate of 10 mA g<sup>-1</sup> are shown in

Figure 3(a) and (b), respectively. On first charge to 4.3 V at 10 mA g<sup>-1</sup>, Air-Na<sub>0.67</sub>Mn<sub>0.9</sub>Zn<sub>0.1</sub>O<sub>2</sub> shows a plateau beyond 4.0 V with a small plateau observed upon subsequent discharge. This coincides with the differential capacity plot which exhibits two small irreversible oxidation peaks at 4.14 and 4.19 V and a third oxidation peak at 4.24 V coupled with a small reduction peak at 4.19 V.

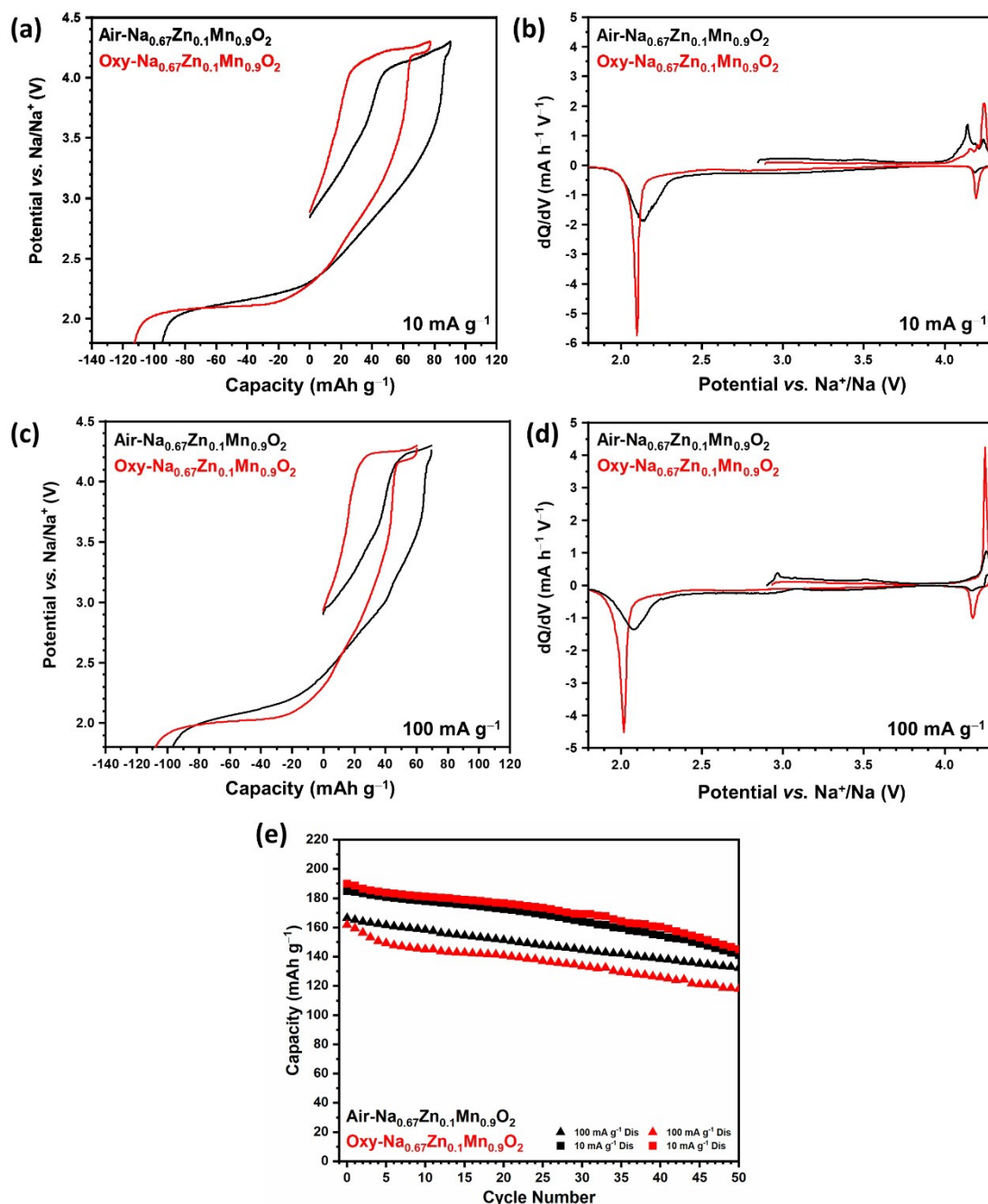


**Figure 3.** Charge/discharge curves of Air-Na<sub>0.67</sub>Mn<sub>0.9</sub>Zn<sub>0.1</sub>O<sub>2</sub> (black) and Oxy-Na<sub>0.67</sub>Mn<sub>0.9</sub>Zn<sub>0.1</sub>O<sub>2</sub> (red) half-cells cycled at 30 °C between 1.8–4.3 V, showing the first cycle at a rate of (a) 10 mA g<sup>-1</sup> and (c) 100 mA g<sup>-1</sup>. The differential capacity versus voltage plots of Air-Na<sub>0.67</sub>Mn<sub>0.9</sub>Zn<sub>0.1</sub>O<sub>2</sub> (black) and Oxy-Na<sub>0.67</sub>Mn<sub>0.9</sub>Zn<sub>0.1</sub>O<sub>2</sub> (red) half-cells corresponding to the first cycle in the voltage range 1.8–4.3 V at a rate of (b) 10 mA g<sup>-1</sup> and (d) 100 mA g<sup>-1</sup>. (e) Galvanostatic cycling performance of Air-Na<sub>0.67</sub>Mn<sub>0.9</sub>Zn<sub>0.1</sub>O<sub>2</sub> (black) and Oxy-Na<sub>0.67</sub>Mn<sub>0.9</sub>Zn<sub>0.1</sub>O<sub>2</sub> (red), cycled between 1.8–4.3 V. Square-shaped symbols represent discharge capacities of cells cycled at a rate of 10 mA g<sup>-1</sup> and triangle-shaped symbols represent discharge capacities of cells cycled at a rate of 100 mA g<sup>-1</sup>.

As for Oxy-Na<sub>0.67</sub>Mn<sub>0.9</sub>Zn<sub>0.1</sub>O<sub>2</sub>, this exhibits two small irreversible peaks at 4.16 and 4.20 V and a reversible redox couple at 4.2 V with a small polarization of 50 mV. The oxidation and reduction peaks at 4.24 and 4.19 V observed for Oxy-Na<sub>0.67</sub>Mn<sub>0.9</sub>Zn<sub>0.1</sub>O<sub>2</sub> are sharper and more intense than those from Air-Na<sub>0.67</sub>Mn<sub>0.9</sub>Zn<sub>0.1</sub>O<sub>2</sub>, coincident with the presence of transition metal vacancies in Oxy-Na<sub>0.67</sub>Mn<sub>0.9</sub>Zn<sub>0.1</sub>O<sub>2</sub>. The oxygen redox processes of Air-Na<sub>0.67</sub>Mn<sub>0.9</sub>Zn<sub>0.1</sub>O<sub>2</sub> and Oxy-Na<sub>0.67</sub>Mn<sub>0.9</sub>Zn<sub>0.1</sub>O<sub>2</sub>

show a large voltage hysteresis associated with Zn doping as has been observed previously in the corresponding P2-type phase.<sup>[20]</sup> Previously, large voltage hysteresis associated with the oxygen redox process has been attributed to the migration of the substituted element from the transition-metal layers and honeycomb-ordering of the transition metal layer facilitates in-plane migration of Mn.<sup>[17,19,20]</sup> As discussed earlier, Air-Na<sub>0.67</sub>Mn<sub>0.9</sub>Zn<sub>0.1</sub>O<sub>2</sub> and Oxy-Na<sub>0.67</sub>Mn<sub>0.9</sub>Zn<sub>0.1</sub>O<sub>2</sub> will tend to adopt

honeycomb-type cation ordering as revealed by the powder neutron diffraction data of Air-Na<sub>0.67</sub>Mn<sub>0.75</sub>Zn<sub>0.25</sub>O<sub>2</sub> (Figure S2) and since Zn is substituted for Mn, it is likely that in-plane migration of Mn and/or the partial reversible migration of Zn between transition-metal and Na<sup>+</sup> ion layers may occur in the high-voltage region, leading to the observed voltage hysteresis.<sup>[20,35]</sup>

Increasing the upper voltage cut off to 4.3 V (Figure 3) results in a greater capacity compared to the smaller voltage range (1.8–3.8 V, Figure 2), arising from the oxygen redox. However, it is challenging to quantify the discharge capacity as a function of redox source as the oxygen redox associated with the Zn doping occurs at roughly 2.7 V on discharge, where Mn<sup>3+</sup>/Mn<sup>4+</sup> redox also occurs. Therefore, we evaluated how much of the discharge capacity occurs over the high voltage region, between 3.8–4.3 V. For Air-Na<sub>0.67</sub>Mn<sub>0.9</sub>Zn<sub>0.1</sub>O<sub>2</sub>, 3.5% of the discharge capacity occurs within this voltage window whereas for Oxy-Na<sub>0.67</sub>Mn<sub>0.9</sub>Zn<sub>0.1</sub>O<sub>2</sub>, almost 2.5 times more (8.4%) capacity is observed, arising from oxygen redox due to the presence of transition metal vacancies, demonstrating that the vacancies provide an additional source of capacity derived from oxygen redox. However, cycling over the wider voltage range, 1.8–4.3 V, leads to a reduced capacity retention of 76% for both materials when cycled at a rate of 10 mA g<sup>-1</sup> over 50 cycles. When cycled at the faster rate of 100 mA h g<sup>-1</sup>, the

initial discharge capacity decreases from 185.1 to 166.4 mA h g<sup>-1</sup> for Air-Na<sub>0.67</sub>Mn<sub>0.9</sub>Zn<sub>0.1</sub>O<sub>2</sub> and from 189.9 to 161.8 mA h g<sup>-1</sup> for Oxy-Na<sub>0.67</sub>Mn<sub>0.9</sub>Zn<sub>0.1</sub>O<sub>2</sub> and with reduced capacity retention of 80% and 73% over 50 cycles for Air-Na<sub>0.67</sub>Mn<sub>0.9</sub>Zn<sub>0.1</sub>O<sub>2</sub> and Oxy-Na<sub>0.67</sub>Mn<sub>0.9</sub>Zn<sub>0.1</sub>O<sub>2</sub>, respectively.

Figure 4(a) and (b) show the differential capacity versus voltage plots of Air-Na<sub>0.67</sub>Mn<sub>0.9</sub>Zn<sub>0.1</sub>O<sub>2</sub> and Oxy-Na<sub>0.67</sub>Mn<sub>0.9</sub>Zn<sub>0.1</sub>O<sub>2</sub> during the second, third, fifth, 10<sup>th</sup>, 20<sup>th</sup> and 30<sup>th</sup> cycles, cycled at a rate of 10 mA g<sup>-1</sup>. On further cycling of Air-Na<sub>0.67</sub>Mn<sub>0.9</sub>Zn<sub>0.1</sub>O<sub>2</sub>, the redox process above 4.1 V diminishes. By contrast, for Oxy-Na<sub>0.67</sub>Mn<sub>0.9</sub>Zn<sub>0.1</sub>O<sub>2</sub>, this high voltage process persists and exhibits a small voltage hysteresis of 80 mV even after 30 cycles, thereby demonstrating enhanced oxygen redox stability due to the presence of transition metal vacancies. Based on these observations, it appears that the presence of Zn<sup>2+</sup> ions in P3-type Air-Na<sub>0.67</sub>Mn<sub>0.9</sub>Zn<sub>0.1</sub>O<sub>2</sub> and Oxy-Na<sub>0.67</sub>Mn<sub>0.9</sub>Zn<sub>0.1</sub>O<sub>2</sub>, as compared to other P3-type materials like Na<sub>0.67</sub>Mn<sub>0.8</sub>Mg<sub>0.2</sub>O<sub>2</sub>, results in a more stable framework.<sup>[12,22]</sup>

To clarify the voltage associated with the oxygen redox process, a series of cyclic voltammograms were collected at a scan rate of 30 μV s<sup>-1</sup> from OCV to progressively higher positive potentials of 3.3 V, 3.8 V, and 4.3 V, fixing the lower voltage cut-off potential at 1.8 V for each cycle. The cyclic voltammograms for Air-Na<sub>0.67</sub>Mn<sub>0.9</sub>Zn<sub>0.1</sub>O<sub>2</sub> and Oxy-Na<sub>0.67</sub>Mn<sub>0.9</sub>Zn<sub>0.1</sub>O<sub>2</sub> are shown in Figure 4(c) and (d), respectively. Upon charging Air-

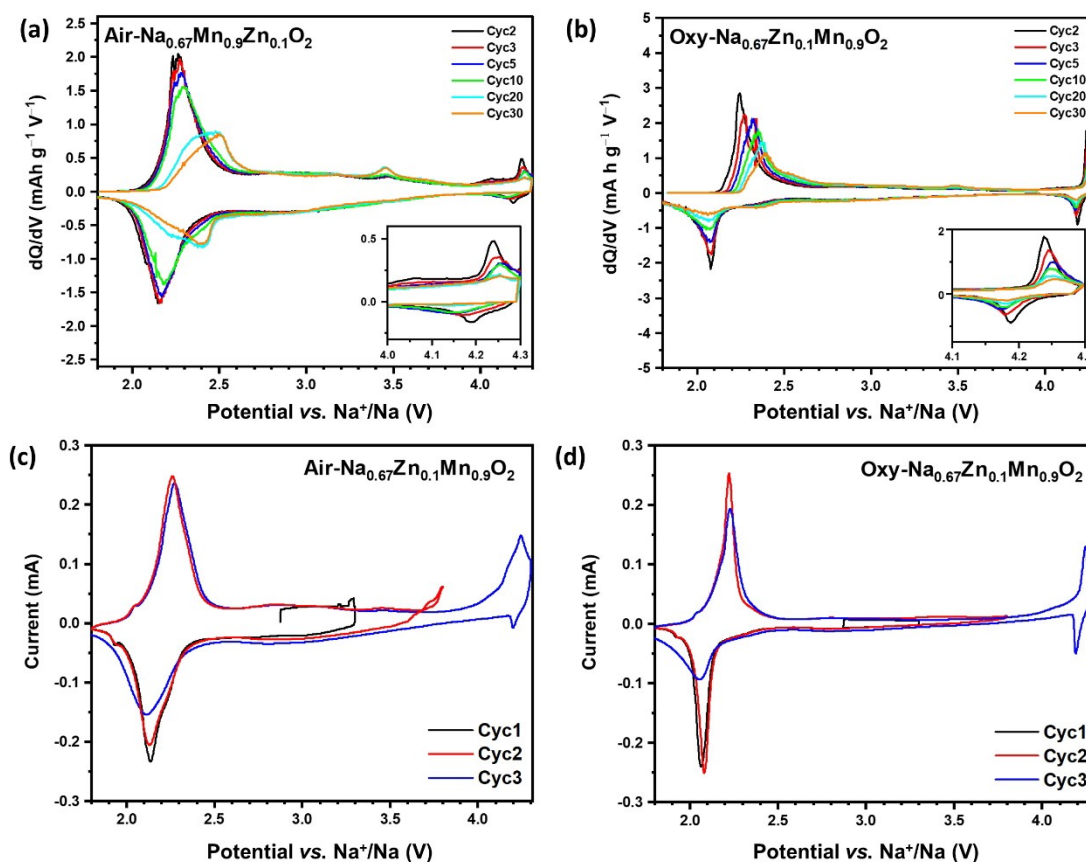


**Figure 4.** Derivative  $dQ/dV$  plots of (a) Air-Na<sub>0.67</sub>Mn<sub>0.9</sub>Zn<sub>0.1</sub>O<sub>2</sub> and (b) Oxy-Na<sub>0.67</sub>Mn<sub>0.9</sub>Zn<sub>0.1</sub>O<sub>2</sub>, collected at 30 °C between 1.8 V and 4.3 V at a rate of 10 mA g<sup>-1</sup> showing the second (black), third (red), fifth (blue), tenth (green), twentieth (cyan) and thirtieth (orange) cycles. Voltammetric analysis for (c) Air-Na<sub>0.67</sub>Mn<sub>0.9</sub>Zn<sub>0.1</sub>O<sub>2</sub> and (d) Oxy-Na<sub>0.67</sub>Mn<sub>0.9</sub>Zn<sub>0.1</sub>O<sub>2</sub> at a scan rate of 30 μV s<sup>-1</sup>.

$\text{Na}_{0.67}\text{Mn}_{0.9}\text{Zn}_{0.1}\text{O}_2$  from OCV to 3.3 V and then discharging to 1.8 V, two reduction peaks are observed at 1.93 and 2.13 V. On subsequent cycling, two oxidation peaks are observed at 2.04 and 2.26 V, coupled with the reduction peaks at 1.94 and 2.13 V, consistent with the  $\text{Mn}^{3+}/\text{Mn}^{4+}$  redox couple. On the third cycle, an oxidation peak at 4.24 V is coupled to a small reduction peak at 4.20 V and a second smaller, broad reduction peak at around 2.8 V, arising from oxygen redox associated with Zn doping. Air- $\text{Na}_{0.67}\text{Mn}_{0.8}\text{Zn}_{0.2}\text{O}_2$  exhibits essentially the same processes but a more pronounced reduction peak at 2.76 V, as shown in Figure S3, due to the presence of more  $\text{Zn}^{2+}$  ions. For Oxy- $\text{Na}_{0.67}\text{Mn}_{0.9}\text{Zn}_{0.1}\text{O}_2$ , sharp oxidation and reduction peaks are observed on the second cycle at 2.22 and 2.08 V, respectively, associated with the  $\text{Mn}^{3+}/\text{Mn}^{4+}$  redox couple. Increasing the voltage range to 4.3 V, reveals a sharp redox couple with oxidation and reduction peaks at 4.24 and 4.19 V, respectively, showing small polarization which may be associated with the presence of transition metal vacancies in the Oxy- $\text{Na}_{0.67}\text{Mn}_{0.9}\text{Zn}_{0.1}\text{O}_2$  material.

### 2.3. Structural evolution of Air- $\text{Na}_{0.67}\text{Mn}_{0.9}\text{Zn}_{0.1}\text{O}_2$ and Oxy- $\text{Na}_{0.67}\text{Mn}_{0.9}\text{Zn}_{0.1}\text{O}_2$

To reveal the structural changes of Air- $\text{Na}_{0.67}\text{Mn}_{0.9}\text{Zn}_{0.1}\text{O}_2$  and Oxy- $\text{Na}_{0.67}\text{Mn}_{0.9}\text{Zn}_{0.1}\text{O}_2$  during electrochemical cycling, ex-situ PXRD studies were performed. PXRD patterns were collected on the Air- $\text{Na}_{0.67}\text{Mn}_{0.9}\text{Zn}_{0.1}\text{O}_2$  and Oxy- $\text{Na}_{0.67}\text{Mn}_{0.9}\text{Zn}_{0.1}\text{O}_2$  electrodes at various states of charge and discharge, are shown in Figure S4 (a) and (b), respectively. Rietveld refinements were performed, and the fits obtained are shown in Figure 5. The refined structural parameters are given in Tables S3 and S4 for Air- $\text{Na}_{0.67}\text{Mn}_{0.9}\text{Zn}_{0.1}\text{O}_2$  and Oxy- $\text{Na}_{0.67}\text{Mn}_{0.9}\text{Zn}_{0.1}\text{O}_2$ , respectively.

The PXRD patterns of Air- $\text{Na}_{0.67}\text{Mn}_{0.9}\text{Zn}_{0.1}\text{O}_2$  and Oxy- $\text{Na}_{0.67}\text{Mn}_{0.9}\text{Zn}_{0.1}\text{O}_2$  charged to 3.8 V (CH3.8 V) and 4.3 V (CH4.3 V) were fitted in the  $R3m$  space group, demonstrating that the P3 structure was maintained upon  $\text{Na}^+$  ion extraction. On charging, the  $a$  unit cell parameter, which is dominated by the TM–O bond length, contracted for both materials, as expected from the oxidation of residual  $\text{Mn}^{3+}$  to  $\text{Mn}^{4+}$  ions. By contrast the  $c$  unit cell parameter expanded slightly for both materials because the screening effect of  $\text{Na}^+$  ions is reduced upon  $\text{Na}^+$  ion extraction, resulting in increased Coulombic repulsion. This results in a minimal reduction of the unit cell volume for Air- $\text{Na}_{0.67}\text{Mn}_{0.9}\text{Zn}_{0.1}\text{O}_2$  (2.06%) and Oxy- $\text{Na}_{0.67}\text{Mn}_{0.9}\text{Zn}_{0.1}\text{O}_2$  (1.38%), after charge to 4.3 V. There was only a hint of conversion to the O3 phase when Air- $\text{Na}_{0.67}\text{Mn}_{0.9}\text{Zn}_{0.1}\text{O}_2$  was charged to 4.3 V whilst for Oxy- $\text{Na}_{0.67}\text{Mn}_{0.9}\text{Zn}_{0.1}\text{O}_2$ , the P3 phase was fully maintained.

Upon  $\text{Na}^+$  ion insertion, the PXRD patterns of Air- $\text{Na}_{0.67}\text{Mn}_{0.9}\text{Zn}_{0.1}\text{O}_2$  and Oxy- $\text{Na}_{0.67}\text{Mn}_{0.9}\text{Zn}_{0.1}\text{O}_2$  discharged to 1.8 V after charge to 3.8 V (CYC3.8V) reveals a transformation to the O'3 phase, with only a minor amount of the P3 phase remaining for Air- $\text{Na}_{0.67}\text{Mn}_{0.9}\text{Zn}_{0.1}\text{O}_2$ , but complete conversion to the O'3 phase for Oxy- $\text{Na}_{0.67}\text{Mn}_{0.9}\text{Zn}_{0.1}\text{O}_2$ . After discharge to 1.8 V following charge to 4.3 V (CYC4.3V), both materials showed complete transformation to the O'3 phase (space group  $C2/m$ ).

The ratio between the unit cell parameters,  $a/b$  for the Air- $\text{Na}_{0.67}\text{Mn}_{0.9}\text{Zn}_{0.1}\text{O}_2$  and Oxy- $\text{Na}_{0.67}\text{Mn}_{0.9}\text{Zn}_{0.1}\text{O}_2$  electrodes after discharge to 1.8 V are 1.86 and 1.89, respectively. While these values are greater than  $\sqrt{3}$ , and indicative of Jahn-Teller distortion which causes structural irreversibility, it can be assumed that this distortion has been suppressed through Zn-doping.<sup>[36]</sup>  $\text{Na}^+$  ion insertion into the P3 phase causes Coulombic repulsion between the Na and Mn cations and the structural transformation *via* layer gliding to O'3 occurs to minimize this repulsion.<sup>[36]</sup> In addition, these data show that the presence of transition metal vacancies does not influence the structural evolution since the same structural transformation was observed for Air- $\text{Na}_{0.67}\text{Mn}_{0.9}\text{Zn}_{0.1}\text{O}_2$  and Oxy- $\text{Na}_{0.67}\text{Mn}_{0.9}\text{Zn}_{0.1}\text{O}_2$ . The phase transformation (P3→O'3) was also accompanied by an expansion in the unit cell volume for Air- $\text{Na}_{0.67}\text{Mn}_{0.9}\text{Zn}_{0.1}\text{O}_2$  (4.01%) and Oxy- $\text{Na}_{0.67}\text{Mn}_{0.9}\text{Zn}_{0.1}\text{O}_2$  (4.29%). Mariyappan *et al.* reported a similar small change in the unit cell volume for Zn-doped  $\text{NaNi}_{0.45}\text{Zn}_{0.05}\text{Mn}_{0.4}\text{Ti}_{0.1}\text{O}_2$ , compared with the large unit cell volume reduction (> 25%) observed for  $\text{NaNi}_{0.5}\text{Mn}_{0.4}\text{Ti}_{0.1}\text{O}_2$ .<sup>[37]</sup> Therefore, it is reasonable to assume that the presence of  $\text{Zn}^{2+}$  ions suppresses the unit cell volume changes on cycling, resulting in enhanced cyclability (Figure 4).

### 2.4. Evolution of electronic structure of Air- $\text{Na}_{0.67}\text{Mn}_{0.9}\text{Zn}_{0.1}\text{O}_2$ and Oxy- $\text{Na}_{0.67}\text{Mn}_{0.9}\text{Zn}_{0.1}\text{O}_2$

To further verify the oxygen redox process beyond 4.10 V, the oxidation states of manganese during the first cycle were investigated by ex-situ X-ray absorption spectroscopy (XAS). Data were collected on the Air- $\text{Na}_{0.67}\text{Mn}_{0.9}\text{Zn}_{0.1}\text{O}_2$  and Oxy- $\text{Na}_{0.67}\text{Mn}_{0.9}\text{Zn}_{0.1}\text{O}_2$  electrodes at various states of charge and discharge, Figure S4 (a) and (b), respectively, as well as manganese foil,  $\text{Mn}_2\text{O}_3$  and  $\text{MnO}_2$  reference compounds with manganese formal oxidation states of 0, +3, and +4, respectively. The Mn K-edge X-ray absorption near edge structure (XANES) spectra for  $\text{Mn}_2\text{O}_3$  and  $\text{MnO}_2$  reference compounds and the Air- $\text{Na}_{0.67}\text{Mn}_{0.9}\text{Zn}_{0.1}\text{O}_2$  electrodes are compared in Figure 6(a) and the Oxy- $\text{Na}_{0.67}\text{Mn}_{0.9}\text{Zn}_{0.1}\text{O}_2$  electrodes in Figure 6(c). Comparing the reference compound  $\text{MnO}_2$  to the XANES spectrum obtained for pristine Air- $\text{Na}_{0.67}\text{Mn}_{0.9}\text{Zn}_{0.1}\text{O}_2$  (Figure 6(b)), it is evident that the pristine material predominantly contains  $\text{Mn}^{4+}$  ions with contributions from  $\text{Mn}^{3+}$  which agrees with the average oxidation state determined from Rietveld analysis. The XANES data for the Air- $\text{Na}_{0.67}\text{Mn}_{0.9}\text{Zn}_{0.1}\text{O}_2$  electrodes after charging to 3.8 V and 4.3 V, essentially overlap with those of pristine Air- $\text{Na}_{0.67}\text{Mn}_{0.9}\text{Zn}_{0.1}\text{O}_2$ , indicating little participation of Mn ions in the charge transfer reaction. Figure 6(b) reveals small shifts towards higher energy upon charging, indicating the oxidation of residual  $\text{Mn}^{3+}$  to  $\text{Mn}^{4+}$  ions. At the end of discharge after charging to 3.8 V and 4.3 V, the XANES spectra shift slightly to lower edge energies, as compared to the pristine material, demonstrating the expected reduction of Mn ions.

The Oxy- $\text{Na}_{0.67}\text{Mn}_{0.9}\text{Zn}_{0.1}\text{O}_2$  electrodes (Figure 6(c)) present the same trend, suggesting that the evolution of the Mn oxidation state is the same and uninfluenced by the presence

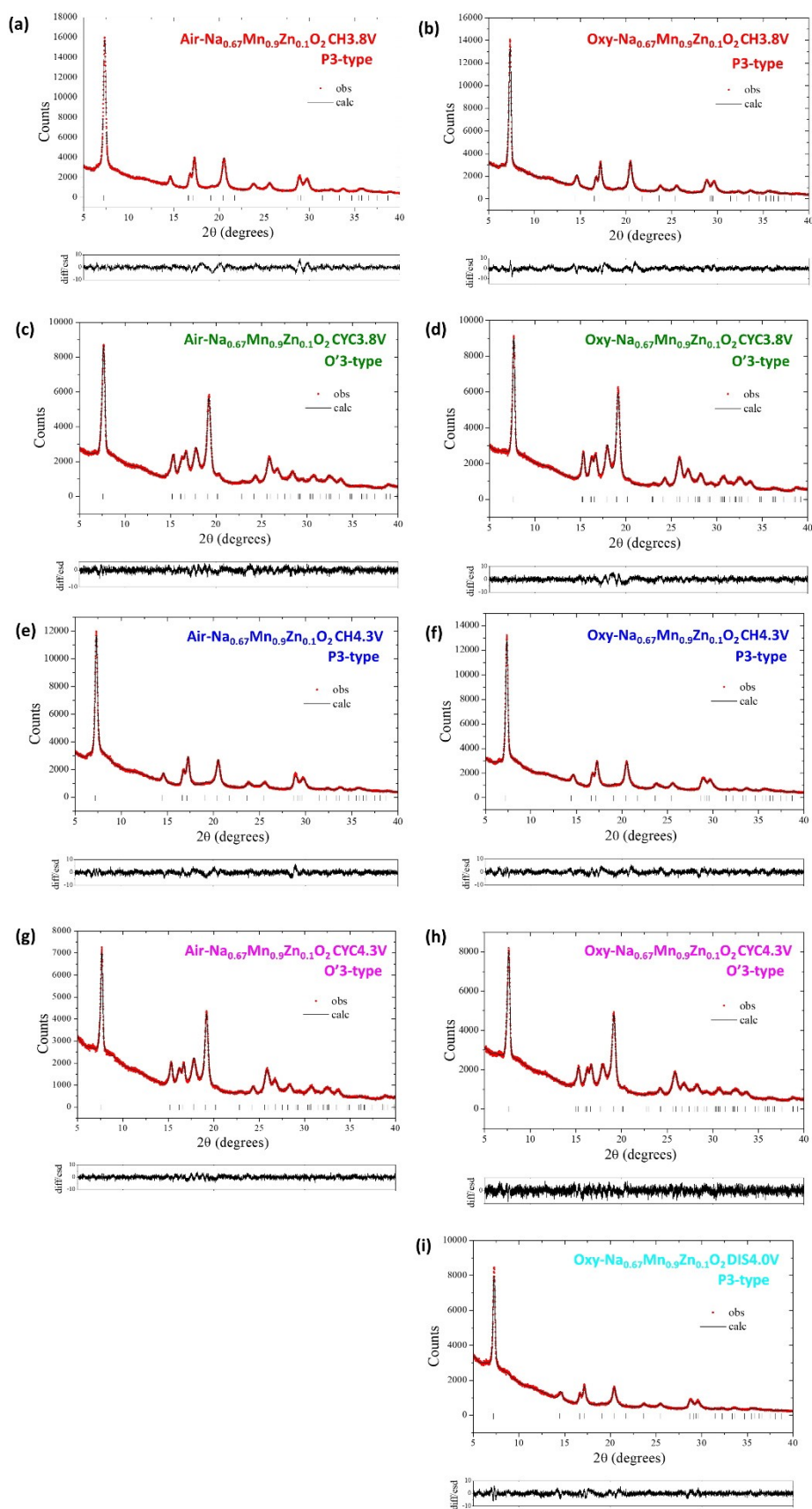


**Figure 5.** Laboratory X-ray Rietveld fits of  $\text{Air-Na}_{0.67}\text{Mn}_{0.9}\text{Zn}_{0.1}\text{O}_2$  (a) charged to 3.8 V, (c) cycled between 1.8 V and 3.8 V, (e) charged to 4.3 V, (g) cycled between 1.8 V and 4.3 V, and  $\text{Oxy-Na}_{0.67}\text{Mn}_{0.9}\text{Zn}_{0.1}\text{O}_2$  (b) charged to 3.8 V, (d) cycled between 1.8 V and 3.8 V, (f) charged to 4.3 V, (h) cycled between 1.8 V and 4.3 V, and (i) discharged to 4.0 V. Observed data points are shown in red, with the fitted profiles in black. Tick marks indicate allowed reflections.



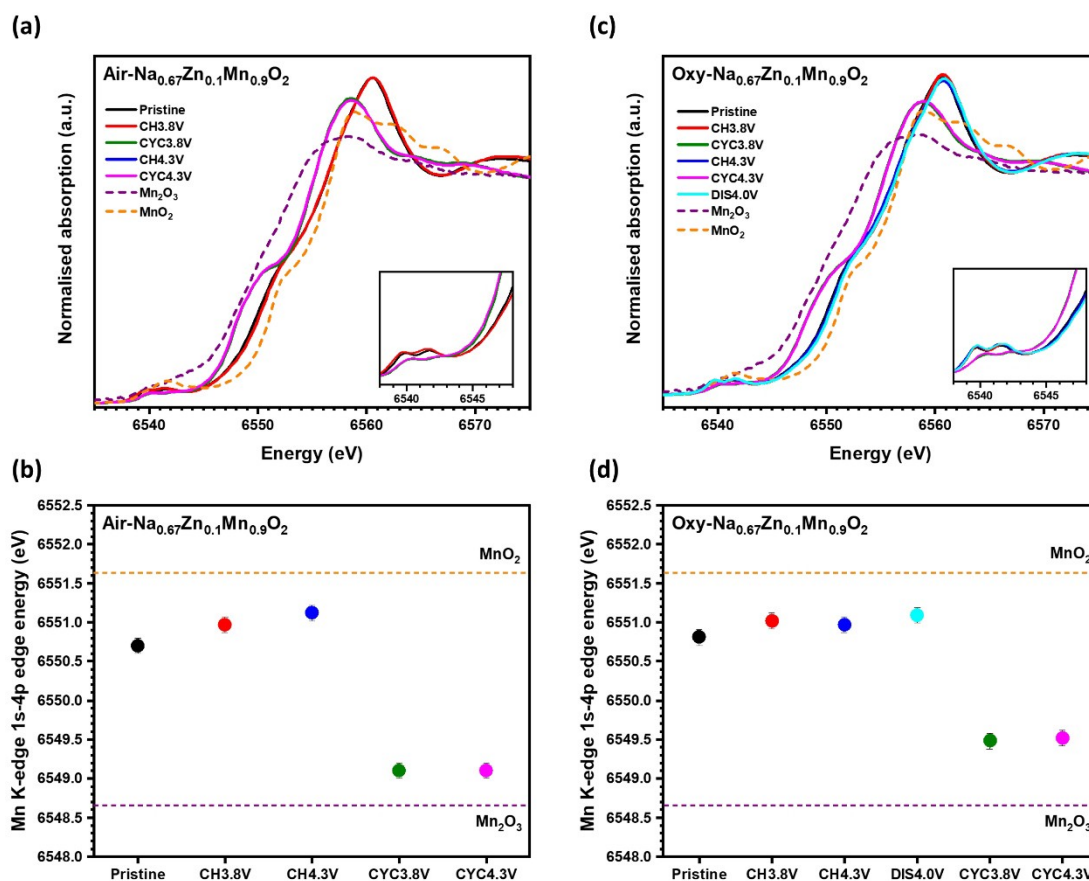


**Figure 6.** Mn K-edge XANES normalised spectra of the ex-situ (a) Air- $\text{Na}_{0.67}\text{Mn}_{0.9}\text{Zn}_{0.1}\text{O}_2$  and (c) Oxy- $\text{Na}_{0.67}\text{Mn}_{0.9}\text{Zn}_{0.1}\text{O}_2$  at various states of charge and discharge compared to the reference materials  $\text{Mn}_2\text{O}_3$  ( $\text{Mn}^{3+}$ ) and  $\text{MnO}_2$  ( $\text{Mn}^{4+}$ ). Mn K-edge energy (at half height) as a function of charge/discharge for (b) Air- $\text{Na}_{0.67}\text{Mn}_{0.9}\text{Zn}_{0.1}\text{O}_2$  and (d) Oxy- $\text{Na}_{0.67}\text{Mn}_{0.9}\text{Zn}_{0.1}\text{O}_2$ .

of transition metal vacancies. Given that  $\text{Zn}^{2+}$  ions are electrochemically inactive,<sup>[20]</sup> these data confirm that the  $\text{Mn}^{3+}/\text{Mn}^{4+}$  redox couple is active below 3.8 V, and suggests that lattice oxygen participates in the charge compensation mechanism between 3.8 and 4.3 V. These results coincide with earlier work on other P3-type manganese-based sodium layered oxides.<sup>[12,22]</sup>

To provide direct evidence of the participation of oxygen anions in the charge compensation mechanism over the high voltage region, ex-situ oxygen K-edge soft X-ray absorption spectroscopy (SXAS) and resonant inelastic X-ray scattering (RIXS) data were collected on electrodes of Air- $\text{Na}_{0.67}\text{Mn}_{0.9}\text{Zn}_{0.1}\text{O}_2$  and Oxy- $\text{Na}_{0.67}\text{Mn}_{0.9}\text{Zn}_{0.1}\text{O}_2$  at the same states of charge and discharge as were studied for the Mn K-edge spectra. SXAS spectra were collected in the partial fluorescence yield (PFY), probing to depths of approximately 100 nm.<sup>[38]</sup> The SXAS spectra of the oxygen K-edge in the bulk sensitive PFY mode for Air- $\text{Na}_{0.67}\text{Mn}_{0.9}\text{Zn}_{0.1}\text{O}_2$  and Oxy- $\text{Na}_{0.67}\text{Mn}_{0.9}\text{Zn}_{0.1}\text{O}_2$  are shown in Figure 7(a) and (d), respectively. The O K-edge spectra can be divided into three regions: (i) the pre-edge region (below 533 eV) which is characteristic of the electronic transition from the O 1s states to the unoccupied O 2p states hybridized with transition metal 3d states (O 2p-TM 3d), (ii) an absorption peak at 534 eV, assigned to the unoccupied O 2p states hybridized with Na 3p states (O 2p-Na 3p), showing changes in its intensity

upon charge/discharge (i.e. Na content),<sup>[39–41]</sup> and (iii) broad peaks beyond 535 eV which can be attributed to the electronic transitions to the O 2p states hybridized with transition metal 4s and 4p states (O 2p-TM 4sp).

The Mn L-edge SXAS and RIXS show that Mn ions do not participate significantly in the charge compensation upon initial charge (see Figures S5 and S6). The pristine material shows a predominantly  $\text{Mn}^{4+}$  signature with minute changes stemming from  $\text{Mn}^{3+}$  contributions, which is in good agreement with Mn K-edge XANES considering the differences in probing depth. By contrast O K-edge SXAS and RIXS show stronger indications of oxygen ion activity, contributing to the initial charge compensation, particularly above 3.8 V. Below we discuss our findings for oxygen in more detail.

The O K-edge SXAS shows absorption peaks at ca. 530 and 532 eV relate to the transitions to unoccupied hybridized states of O 2p-TM  $t_{2g}$  and O 2p-TM  $e_g$ , respectively.<sup>[42–44]</sup> The integral of the pre-edge region (526–532.5 eV) relates to changes in the density of empty states above the Fermi level which is influenced by the oxidation state of the Mn and the covalency of the O 2p band.<sup>[18]</sup>

The integrated intensity of the pre-edge region, relative to the pristine material for Air- $\text{Na}_{0.67}\text{Mn}_{0.9}\text{Zn}_{0.1}\text{O}_2$  and Oxy- $\text{Na}_{0.67}\text{Mn}_{0.9}\text{Zn}_{0.1}\text{O}_2$  are shown in Figure 7(b) and (e), respectively.

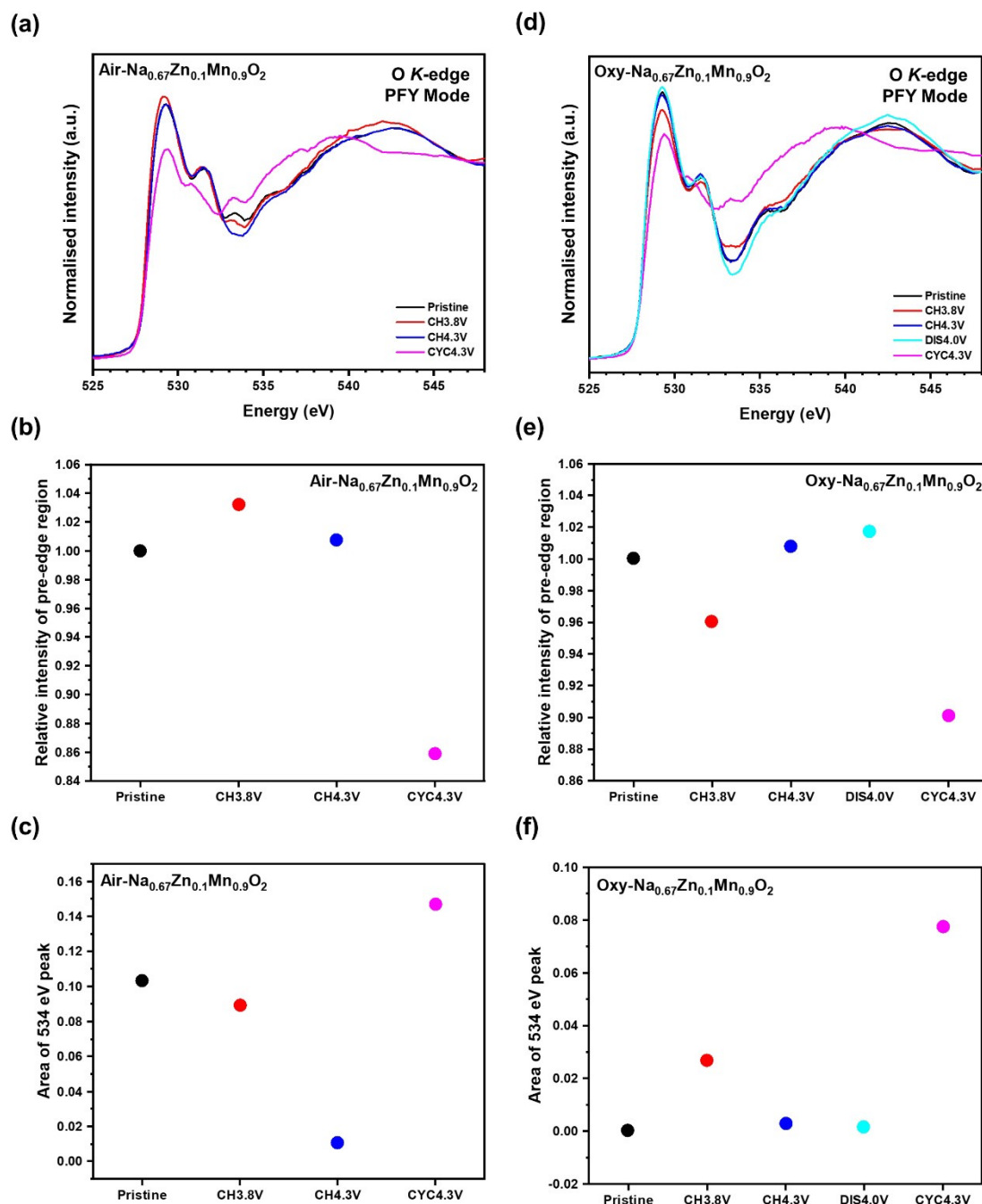


**Figure 7.** Normalised O K-edge SXAS spectra at various states of charge and discharge, collected in PFY mode for (a) Air- $\text{Na}_{0.67}\text{Mn}_{0.9}\text{Zn}_{0.1}\text{O}_2$  and (d) Oxy- $\text{Na}_{0.67}\text{Mn}_{0.9}\text{Zn}_{0.1}\text{O}_2$ . The integrated intensity of the pre-edge feature (526–532.5 eV) for the O K-edge SXAS, relative to the pristine phase for (b) Air- $\text{Na}_{0.67}\text{Mn}_{0.9}\text{Zn}_{0.1}\text{O}_2$  and (e) Oxy- $\text{Na}_{0.67}\text{Mn}_{0.9}\text{Zn}_{0.1}\text{O}_2$ . The peak area at 534 eV for the O K-edge SXAS for (c) Air- $\text{Na}_{0.67}\text{Mn}_{0.9}\text{Zn}_{0.1}\text{O}_2$  and (f) Oxy- $\text{Na}_{0.67}\text{Mn}_{0.9}\text{Zn}_{0.1}\text{O}_2$ .

Figure 7(b) reveals changes in the intensity relative to the pristine phase during cycling. Upon charging these intensity variations are observed to be small and mainly due to effects from hybridization between the O 2p and TM 3d states and structural evolution. On discharge to 1.8 V after charge to 4.3 V, the intensity decreases substantially which suggests that the electron-holes of the oxygen 2p states are repopulated and is consistent with the reduction to  $\text{Mn}^{3+}$  (Figure 6). As for Figure 7(e), upon charge to 4.3 V the intensity increases, indicating an oxidation which implies the removal of electrons

from oxygen, agreeing with the electrochemical data (Figure 3). As with Figure 7(b), at the end of discharge to 1.8 V, the intensity decreases considerably, demonstrating the reversibility of the oxygen-redox reaction.

The evolution of the intensity of the O 2p-Na 3p peak (*ca.* 534 eV) upon charge/discharge is shown in Figure 7(c) and (f) for Air- $\text{Na}_{0.67}\text{Mn}_{0.9}\text{Zn}_{0.1}\text{O}_2$  and Oxy- $\text{Na}_{0.67}\text{Mn}_{0.9}\text{Zn}_{0.1}\text{O}_2$ . Figure 7(c) and (f) show that the O 2p-Na 3p peak intensity dips to a minimum at 4.3 V and rises sharply upon discharge, which follows the degree of sodiation. This behaviour is intriguing

because it also would be compatible with the creation and refilling of electron holes due to pure oxygen redox (*i.e.* not related to direct Mn–O bonding). Depopulation of a nonbonding orbital is thus expected to occur above 3.8 V.

Oxygen K-edge RIXS has previously proved to be a powerful probe for studying the effect of oxygen redox in batteries,<sup>[12]</sup> since it offers a site-specific picture of electronic structure evolution of the occupied O bands by carefully selecting a range of excitation energies. Figure S6 shows that, for the excitation energy range 528–532.5 eV, there are only relatively small changes during charge. This is not unexpected since this pre-peak range probes Mn–O hybridized states. By contrast, at excitation energy 533 eV, shown in Figure 8, we observe significant spectral changes in O K-RIXS for both Air- $\text{Na}_{0.67}\text{Mn}_{0.9}\text{Zn}_{0.1}\text{O}_2$  and Oxy- $\text{Na}_{0.67}\text{Mn}_{0.9}\text{Zn}_{0.1}\text{O}_2$ . At 533 eV, *i.e.*, just above the pre-peak range valence states are probed that are not related to Mn–O hybridization but instead to other possible O-bands, in particular nonbonding orbitals. The significant shifting of spectral weight of the oxygen main band (features B and C) during the entire charge process reveals that oxygen states are being reordered throughout the entire initial charge process despite the practically unchanged Mn-oxidation state. A nonbonding state directly revealing reversible pure oxygen redox should however manifest as an intensity drop between 3.8 V and 4.3 V (red-to-blue traces) followed by an intensity rise upon discharge to 1.8 V (blue-to-magenta traces). This criterion is indeed fulfilled (only) by the small near-elastic peak at 533 eV for both Air- $\text{Na}_{0.67}\text{Mn}_{0.9}\text{Zn}_{0.1}\text{O}_2$  and Oxy- $\text{Na}_{0.67}\text{Mn}_{0.9}\text{Zn}_{0.1}\text{O}_2$  (see inset Figure 8).

This corresponds nicely to a situation where states very close to the top of the valence band that mix very little with Mn

or  $\text{Zn}^{15}$  become excited just across the Fermi level. Assigning the near-elastic-peak intensity to the relative population of the nonbonding states is also supported in view of its correlation with the degree of sodiation, especially at high voltages where “pure” oxygen redox is expected. Given the present instrumental resolving power, it is difficult to discern any detailed differences between Air- $\text{Na}_{0.67}\text{Mn}_{0.9}\text{Zn}_{0.1}\text{O}_2$  and Oxy- $\text{Na}_{0.67}\text{Mn}_{0.9}\text{Zn}_{0.1}\text{O}_2$  in the spectra, but these results point the way for future more detailed O K-RIXS studies of related systems.

## 2.5. Comparison with Mg substitution

In this study we have presented a new P3-type  $\text{Na}_{0.67}\text{Mn}_{0.9}\text{Zn}_{0.1}\text{O}_2$  phase, *via* the partial substitution of Mn by an electrochemically inert element Zn. This Zn-doped phase behaves in an analogous manner to P3-type  $\text{Na}_{0.67}\text{Mn}_{0.8}\text{Mg}_{0.2}\text{O}_2$ ,<sup>[22]</sup> in which oxygen redox was activated by unpaired O 2p states formed due to the presence of  $\text{Mg}^{2+}$  ions in Air- $\text{Na}_{0.67}\text{Mn}_{0.8}\text{Mg}_{0.2}\text{O}_2$  and Oxy- $\text{Na}_{0.67}\text{Mn}_{0.8}\text{Mg}_{0.2}\text{O}_2$ . Considering the P2-type Zn-substituted  $\text{Na}_{2/3}\text{Zn}_{1/3}\text{Mn}_{2/3}\text{O}_2$  phase, the DFT calculations performed by Bai *et al.* showed that the overlap between the filled Zn 3d<sup>10</sup> and O 2p<sup>2</sup> orbitals is very weak, such that one of the O 2p states is considered a nonbonding state.<sup>[20]</sup> Therefore, this accounts for the similarity of the electrochemical behaviour observed between these Mg- and Zn-substituted materials. To further evaluate the electrochemical performance between Mg- and Zn-substitution, we compared the electrochemical data for Air- $\text{Na}_{0.67}\text{Mn}_{0.9}\text{Zn}_{0.1}\text{O}_2$  and Oxy- $\text{Na}_{0.67}\text{Mn}_{0.9}\text{Zn}_{0.1}\text{O}_2$  (Figure 4(a) and (b)) with 10% Mg-substituted Air- $\text{Na}_{0.67}\text{Mn}_{0.9}\text{Mg}_{0.1}\text{O}_2$  and Oxy- $\text{Na}_{0.67}\text{Mn}_{0.9}\text{Mg}_{0.1}\text{O}_2$  prepared us-

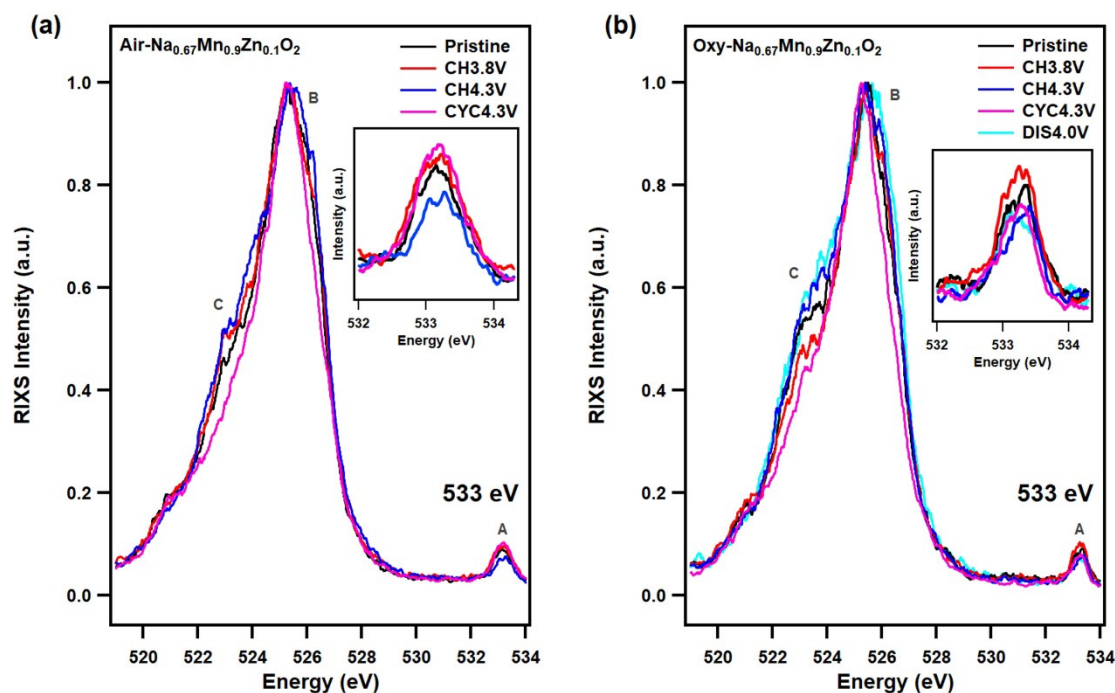


**Figure 8.** Oxygen K-edge RIXS spectra collected at 533.0 eV excitation energy for (a) Air- $\text{Na}_{0.67}\text{Mn}_{0.9}\text{Zn}_{0.1}\text{O}_2$ , and (b) Oxy- $\text{Na}_{0.67}\text{Mn}_{0.9}\text{Zn}_{0.1}\text{O}_2$ , at various states of charge and discharge. The insets show a magnified view of the near-elastic peak intensity.

ing the same synthesis conditions (see Section 2.1) and their  $dQ/dV$  plots are shown in Figure S8 (a) and (b), respectively. These results show almost identical results for the materials synthesised in air (Figures 4(a) and S8 (a)). For the materials synthesised under oxygen, the reversibility of the oxygen redox process centred around 4.2 V, diminishes after 20 cycles for Oxy- $\text{Na}_{0.67}\text{Mn}_{0.9}\text{Mg}_{0.1}\text{O}_2$  (Figure S8 (b)), whereas Oxy- $\text{Na}_{0.67}\text{Mn}_{0.9}\text{Zn}_{0.1}\text{O}_2$  (Figure 4(b)) shows enhanced oxygen redox reversibility at 4.2 V, even after 30 cycles, demonstrating the stabilizing role of  $\text{Zn}^{2+}$  ions in the presence of transition metal vacancies on the oxygen redox reversibility.

As for the structural evolution, the Mg-substituted materials similarly show that the P3 phase is essentially maintained after charge to 4.3 V. Whereas on subsequent discharge to 1.8 V,  $\text{Na}_{0.67}\text{Mn}_{0.8}\text{Mg}_{0.2}\text{O}_2$  reveals reduced transition to the O'3 phase, with 14% and 57% of the P3 phase maintained in Air- $\text{Na}_{0.67}\text{Mn}_{0.8}\text{Mg}_{0.2}\text{O}_2$  and Oxy- $\text{Na}_{0.67}\text{Mn}_{0.8}\text{Mg}_{0.2}\text{O}_2$ , respectively.<sup>[22]</sup> Despite showing complete conversion to the O'3 phase upon  $\text{Na}^+$  insertion, the Zn-substituted materials exhibit enhanced electrochemical performance. Thus, suggesting that substitution of Mn for Zn over Mg, provides a more stable framework for  $\text{Na}^+$  ion insertion/extraction.

### 3. Conclusion

The P3 layered Zn-substituted  $\text{Na}_{0.67}\text{Mn}_{0.9}\text{Zn}_{0.1}\text{O}_2$  material was prepared under both air and oxygen, and contain virtually zero and 6% transition metal vacancies, respectively. Based on the electrochemical tests and electronic structural analysis, both materials exhibit oxygen redox over the high-voltage region (above 3.8 V). In the absence of vacancies,  $\text{Na}_{0.63}\text{Mn}_{0.9}\text{Zn}_{0.1}\text{O}_2$  exhibits large voltage hysteresis from nonbonding O 2p states due to Zn-substitution. As for  $\text{Na}_{0.67}\text{Mn}_{0.86}\text{Zn}_{0.09}\square_{0.06}\text{O}_2$ , the vacancies in the transition metal layer play an important role in producing unpaired O 2p states which enhances the reversibility of oxygen redox. Ultimately, P3- $\text{Na}_{0.67}\text{Mn}_{0.86}\text{Zn}_{0.09}\square_{0.06}\text{O}_2$  delivers greater oxygen redox stability compared to Mg-substituted P3- $\text{Na}_{0.67}\text{Mn}_{0.8}\text{Mg}_{0.2}\text{O}_2$ .<sup>[22]</sup> It has been reported that in O3- $\text{NaNi}_{0.45}\text{Mn}_{0.05}\text{Mn}_{0.4}\text{Ti}_{0.1}\text{O}_2$ , ( $M = \text{Mg}^{2+}, \text{Zn}^{2+}, \text{Cu}^{2+}$ ) the Zn doped material displayed the best cycling stability.<sup>[37]</sup> The lack of d-electrons for  $\text{Mg}^{2+}$ , which can enable  $\pi$ -p bonding with neighbouring oxygen atoms, led to the poorest cyclability, leading to easier Mg migration during cycling. This observation, combined with the results presented here, suggests that the development of Zn-doped materials could lead to oxygen redox active positive electrodes with enhanced stability.

## Experimental Section

### Materials Synthesis

A stoichiometric amount of sodium carbonate ( $\text{Na}_2\text{CO}_3$ , Fischer Chemistry,  $\geq 99.5\%$ ) was dissolved in deionized water, then added drop-wise to a solution of manganese(II) acetate tetrahydrate ( $\text{Mn}(\text{CH}_3\text{CO}_2)_2 \cdot 4\text{H}_2\text{O}$ , Aldrich,  $\geq 99\%$ ) and zinc acetate dihydrate ( $\text{Zn}(\text{CH}_3\text{CO}_2)_2 \cdot 2\text{H}_2\text{O}$ , Sigma-Aldrich,  $\geq 99\%$ ) while stirring. The

solution was stirred for 10 min before the water was removed using a rotary evaporator. The powder was then heated to  $300^\circ\text{C}$  at a rate of  $5^\circ\text{Cmin}^{-1}$  for 12 h. To prepare Air- $\text{Na}_{0.67}\text{Mn}_{1-x}\text{Zn}_x\text{O}_2$  ( $x = 0.1, 0.2, 0.25$ ), the resulting powder was heated to  $625^\circ\text{C}$  at a rate of  $5^\circ\text{Cmin}^{-1}$  for 3 h under air and then quenched. Whereas Oxy- $\text{Na}_{0.67}\text{Mn}_{1-x}\text{Zn}_x\text{O}_2$  ( $x = 0.1, 0.2$ ) was formed by heating the powder to  $625^\circ\text{C}$  at a rate of  $5^\circ\text{Cmin}^{-1}$  under oxygen and cooling to  $50^\circ\text{C}$  at a rate of  $5^\circ\text{Cmin}^{-1}$ . The as-synthesised materials were stored in an argon filled glovebox.

### Characterization

PXRD patterns were collected on a PANalytical Empyrean diffractometer, using  $\text{MoK}\alpha_{1,2}$  radiation ( $\lambda = 0.7107 \text{ \AA}$ ) with a Zr  $\beta$ -filter and X'celerator detector. Data were collected at room temperature in the  $2\theta$  range,  $5.0$ – $40.0^\circ$  over 24 h per scan with a step size of  $0.0084^\circ$  and 4189 steps and a time per step of 20.6 s. Samples were loaded into glass capillaries (0.7 mm diameter) in an argon filled glovebox. A time-of-flight powder neutron diffraction pattern of as-synthesised Air- $\text{Na}_{0.67}\text{Mn}_{0.75}\text{Zn}_{0.25}\text{O}_2$  was obtained on the Polaris diffractometer at ISIS at the Rutherford Appleton Laboratory. Diffraction data were refined using the Rietveld method using Topas Academic V6.<sup>[45]</sup> SEM and EDS analysis were performed on the as-synthesised materials using a Schottky field-emission gun scanning electron microscopy (FEG-SEM, FEI Scios dualbeam) equipped with an EDAX Octane Plus EDS detector for compositional analysis.

### Electrochemical measurements and ex-situ characterization

In order to evaluate the electrochemical properties, positive electrodes were prepared by mixing 75 wt% of the active material, either Air- $\text{Na}_{0.67}\text{Mn}_{1-x}\text{Zn}_x\text{O}_2$  or Oxy- $\text{Na}_{0.67}\text{Mn}_{1-x}\text{Zn}_x\text{O}_2$  ( $x = 0.1, 0.2$ ), with 15 wt% super C65 carbon and 10 wt% Solef 5130 binder (modified polyvinylidene fluoride, PVDF) in n-methyl-2-polyvinylidene which were cast onto aluminium foil using a doctor blade. The dried electrodes were pressed and punched into 13 mm diameter discs before being dried at  $80^\circ\text{C}$  under vacuum. Typical cast electrode loadings were  $2.6 \text{ mg cm}^{-2}$ . CR2325 coin cells were assembled in an argon filled glovebox consisting of a positive disk electrode, sodium metal as a counter/reference electrode, a glass fibre separator (Whatman, GF/F) soaked in electrolyte (1 M  $\text{NaPF}_6$  in ethylene carbonate/diethyl carbonate (1:1 v/v%), Kishida). Galvanostatic charge/discharge cycling, and voltage scans (linear sweep voltammetry) were collected in a temperature-controlled environment at  $30^\circ\text{C}$  using a Biologic BCS-805 battery cycler.

For ex-situ characterization of electrodes 80 wt% of active material (Air- $\text{Na}_{0.67}\text{Mn}_{0.9}\text{Zn}_{0.1}\text{O}_2$  or Oxy- $\text{Na}_{0.67}\text{Mn}_{0.9}\text{Zn}_{0.1}\text{O}_2$ ) was mixed with 20 wt% super C65 carbon, with no binder in an argon filled glovebox for 15 minutes using a pestle and mortar. For PXRD and XAS ex-situ measurements, Swagelok type cells were assembled as described above, using typical powder electrode loadings of  $\sim 30 \text{ mg cm}^{-2}$ , in an argon filled glovebox. Swagelok cells were cycled at  $30^\circ\text{C}$  using a Biologic MacPile II system in galvanostatic mode. The positive electrodes were recovered from the Swagelok cells after cycling in an argon filled glovebox, washed with dry dimethyl carbonate (DMC, Sigma Aldrich,  $\geq 99\%$ ) three times and dried under vacuum overnight. PXRD measurements were carried out as described above. Manganese K-edge (6.5390 keV) XAS spectra were acquired in transmission mode on B18 beamline at Diamond Light Source, UK. The powdered samples (9 mg of active material) were ground for 20 minutes with cellulose (150 mg) and pressed into 13 mm diameter pellets, and then sealed into aluminium bags in an argon filled glovebox. XAS spectra of the manganese metal foil were acquired simultaneously with the

experimental samples. All spectra were acquired in triplicate for each sample. XAS spectra were aligned, merged and normalized using the program Athena.<sup>[46,47]</sup> For ex-situ Mn L-edge and O K-edge SXAS and RIXS measurements, CR2325 coin cells were assembled as described above, except that Solupor membranes were used and soaked with electrolyte. The electrodes were extracted and rinsed with DMC three times and left to dry under vacuum overnight. Spectra were collected at the C-branch of beamline BL27SU at Spring 8 in Japan.<sup>[48]</sup> To obtain SXAS spectra at the Mn L-edge and O K-edge, the PFY and TEY signals were measured simultaneously at a resolution of about 0.1 eV. PFY was detected using an energy dispersive soft X-ray analyser and TEY was recorded using the sample drain current detected by a pico-ammeter. O K-RIXS spectra were collected with a spectrometer of a varied-line-spacing plane cylindrical grating design in first order of diffraction at a combined resolution of about 0.4 eV. The vertical (horizontal) beam size at sample point is about 10  $\mu\text{m}$  (200  $\mu\text{m}$ ).

## Acknowledgements

The authors are grateful for the provision of beam time on B18 at the Diamond Light Source (as part of the Energy Materials Block Allocation Group SP14239) and on BL27SU at Spring 8 (Proposal Number: 2021A1425). We gratefully acknowledge technical support of the Spring 8 user support, particularly beamline scientist Kiyofumi Nitta. This work was supported by the Faraday Institution (grant number FIRG018). The authors gratefully acknowledge support from the Engineering and Physical Sciences Research Council (EPSRC), grants EP/L017008/1, EP/R023751/1 and EP/T019298/1.

## Conflict of Interest

The authors declare no conflict of interest.

## Data Availability Statement

The data that support the findings of this study are available from the corresponding author upon reasonable request.

**Keywords:** Anion redox chemistry · Layered compounds · Positive electrode material · Sodium · Transition metal vacancies

- [1] M. Armand, J.-M. Tarascon, *Nature* **2008**, *451*, 652–657.
- [2] J. Y. Hwang, S. T. Myung, Y. K. Sun, *Chem. Soc. Rev.* **2017**, *46*, 3529–3614.
- [3] N. Yabuuchi, K. Kubota, M. Dahbi, S. Komaba, *Chem. Rev.* **2014**, *114*, 11636–11682.
- [4] N. Tapia-ruiz, A. R. Armstrong, H. Alptekin, M. A. Amores, H. Au, J. Barker, R. Boston, W. R. Brant, J. M. Brittain, Y. Chen, M. Chhowalla, Y. Choi, S. I. R. Costa, M. C. Ribadeneyra, S. A. M. Dickson, E. I. Eweka, J. D. Forero-saboya, C. P. Grey, Z. Li, S. F. L. Mertens, R. Mogensen, L. Monconduit, D. M. C. Ould, R. G. Palgrave, P. Poizot, A. Ponrouch, S. Renault, E. M. Reynolds, A. Rudola, R. Sayers, D. O. Scanlon, S. Sen, V. R. Seymour, B. Silv, G. S. Stone, C. I. Thomas, M. Titirici, J. Tong, T. J. Wood, D. S. Wright, R. Younesi, *J. Phys. Energy* **2021**, *3*, 031503.
- [5] C. Delmas, C. Fouassier, P. Hagenmuller, *Phys. B + C* **1980**, *99*, 81–85.
- [6] S. Kumakura, Y. Tahara, S. Sato, K. Kubota, S. Komaba, *Chem. Mater.* **2017**, *29*, 8958–8962.

- [7] B. Mortemard de Boisse, S. ichi Nishimura, E. Watanabe, L. Lander, A. Tsuchimoto, J. Kikkawa, E. Kobayashi, D. Asakura, M. Okubo, A. Yamada, *Adv. Energy Mater.* **2018**, *8*, S1–S7.
- [8] B. Song, M. Tang, E. Hu, O. J. Borkiewicz, K. M. Wiaderek, Y. Zhang, N. D. Phillip, X. Liu, Z. Shadike, C. Li, L. Song, Y. Y. Hu, M. Chi, G. M. Veith, X. Q. Yang, J. Liu, J. Nanda, K. Page, A. Huq, *Chem. Mater.* **2019**, *31*, 3756–3765.
- [9] Y. Li, X. Wang, Y. Gao, Q. Zhang, G. Tan, Q. Kong, S. Bak, G. Lu, X. Q. Yang, L. Gu, J. Lu, K. Amine, Z. Wang, L. Chen, *Adv. Energy Mater.* **2019**, *9*, 1–9.
- [10] A. Tsuchimoto, X. Shi, K. Kawai, B. M. De Boisse, J. Kikkawa, D. Asakura, M. Okubo, A. Yamada, *Nat. Commun.* **2021**, *12*, 1–7.
- [11] E. Adamczyk, V. Pralong, *Chem. Mater.* **2017**, *29*, 4645–4648.
- [12] E. J. Kim, L. A. Ma, L. C. Duda, D. M. Pickup, A. V. Chadwick, R. Younesi, J. T. S. Irvine, A. Robert Armstrong, *ACS Appl. Energy Mater.* **2020**, *3*, 184–191.
- [13] E. Jeong, K. Mofredj, D. M. Pickup, A. V. Chadwick, J. T. S. Irvine, A. R. Armstrong, *J. Power Sources* **2021**, *481*, 229010 (1–10).
- [14] K. Dai, J. Mao, Z. Zhuo, Y. Feng, W. Mao, G. Ai, F. Pan, Y. Chuang, G. Liu, W. Yang, *Nano Energy* **2020**, *74*, 104831 (1–7).
- [15] C. Hakim, N. Sabi, L. A. Ma, M. Dahbi, D. Brandell, K. Edström, L. C. Duda, I. Saadoun, R. Younesi, *Commun. Chem.* **2020**, *3*, DOI 10.1038/s42004-020-0257-6.
- [16] K. Du, J. Zhu, G. Hu, H. Gao, Y. Li, J. B. Goodenough, *Energy Environ. Sci.* **2016**, *9*, 2575–2577.
- [17] R. A. House, U. Maitra, M. A. Pérez-Osorio, J. G. Lozano, L. Jin, J. W. Somerville, L. C. Duda, A. Nag, A. Walters, K. J. Zhou, M. R. Roberts, P. G. Bruce, *Nature* **2020**, *577*, 502–508.
- [18] U. Maitra, R. A. House, J. W. Somerville, N. Tapia-Ruiz, J. G. Lozano, N. Guerrini, R. Hao, K. Luo, L. Jin, M. A. Pérez-Osorio, F. Massel, D. M. Pickup, S. Ramos, X. Lu, D. E. McNally, A. V. Chadwick, F. Giustino, T. Schmitt, L. C. Duda, M. R. Roberts, P. G. Bruce, *Nat. Chem.* **2018**, *10*, 288–295.
- [19] B. Song, E. Hu, J. Liu, Y. Zhang, X. Q. Yang, J. Nanda, A. Huq, K. Page, *J. Mater. Chem. A* **2019**, *7*, 1491–1498.
- [20] X. Bai, M. Sathiy, B. Mendoza-Sánchez, A. Iadecola, J. Vergnet, R. Dedryvère, M. Saubanère, A. M. Abakumov, P. Rozier, J.-M. Tarascon, *Adv. Energy Mater.* **2018**, *8*, 1802379.
- [21] A. Konarov, J. H. Jo, J. U. Choi, Z. Bakenov, H. Yashiro, J. Kim, S. T. Myung, *Nano Energy* **2019**, *59*, 197–206.
- [22] E. J. Kim, L. A. Ma, D. M. Pickup, A. V. Chadwick, R. Younesi, P. Maughan, J. T. S. Irvine, A. R. Armstrong, *ACS Appl. Energy Mater.* **2020**, DOI 10.1021/acsaem.0c01352.
- [23] H. Xu, J. Zong, X. Liu, *Ionics* **2018**, *24*, 1939–1946.
- [24] X. Wu, G. L. Xu, G. Zhong, Z. Gong, M. J. McDonald, S. Zheng, R. Fu, Z. Chen, K. Amine, Y. Yang, *ACS Appl. Mater. Interfaces* **2016**, *8*, 22227–22237.
- [25] X. Wu, J. Guo, D. Wang, G. Zhong, M. J. McDonald, Y. Yang, *J. Power Sources* **2015**, *281*, 18–26.
- [26] N. Yabuuchi, R. Hara, K. Kubota, J. Paulsen, S. Kumakura, S. Komaba, *J. Mater. Chem. A* **2014**, *2*, 16851–16855.
- [27] B. Song, M. Tang, E. Hu, O. J. Borkiewicz, K. M. Wiaderek, Y. Zhang, N. D. Phillip, X. Liu, Z. Shadike, C. Li, L. Song, Y. Hu, M. Chi, G. M. Veith, X. Q. Yang, J. Liu, J. Nanda, K. Page, A. Huq, *Chem. Mater.* **2019**, *31*, S1–S12.
- [28] A. D. Robertson, A. R. Armstrong, P. G. Bruce, *Chem. Mater.* **2001**, *13*, 2380–2386.
- [29] A. R. Armstrong, A. J. Paterson, A. D. Robertson, P. G. Bruce, *Chem. Mater.* **2002**, *14*, 710–719.
- [30] A. D. Robertson, A. R. Armstrong, A. J. Paterson, M. J. Duncan, P. G. Bruce, *J. Mater. Chem.* **2003**, *13*, 2367–2373.
- [31] X. Liu, G. Zhong, Z. Xiao, B. Zheng, W. Zuo, K. Zhou, *Nano Energy* **2020**, *76*, 104997.
- [32] R. D. Shannon, *Acta Crystallogr.* **1976**, *A32*, 751–767.
- [33] B. Mortemard De Boisse, G. Liu, J. Ma, S. I. Nishimura, S. C. Chung, H. Kiuchi, Y. Harada, J. Kikkawa, Y. Kobayashi, M. Okubo, A. Yamada, *Nat. Commun.* **2016**, *7*, 1–9.
- [34] J. Billaud, G. Singh, A. R. Armstrong, E. Gonzalo, V. Roddatis, M. Armand, T. Rojo, P. G. Bruce, *Energy Environ. Sci.* **2014**, *7*, 1387–1391.
- [35] Y. Wang, L. Wang, H. Zhu, J. Chu, Y. Fang, L. Wu, L. Huang, Y. Ren, C. J. Sun, Q. Liu, X. Ai, H. Yang, Y. Cao, *Adv. Funct. Mater.* **2020**, *30*, 1–9.
- [36] J.-P. Parant, R. Olazcuaga, M. Devalette, C. Fouassier, P. Hagenmuller, *J. Solid State Chem.* **1971**, *3*, 1–11.
- [37] S. Mariyappan, T. Marchandier, F. Rabuel, A. Iadecola, G. Rousse, A. V. Morozov, A. M. Abakumov, J. M. Tarascon, *Chem. Mater.* **2020**, *32*, 1657–1666.

- [38] D. Asakura, E. Hosono, Y. Nanba, H. Zhou, J. Okabayashi, C. Ban, P. A. Glans, J. Guo, T. Mizokawa, G. Chen, A. J. Achkar, D. G. Hawthron, T. Z. Regier, H. Wadati, *AIP Adv.* **2016**, *6*, 035105-1-8.
- [39] W. B. Wu, D. J. Huang, J. Okamoto, A. Tanaka, H. J. Lin, F. C. Chou, A. Fujimori, C. T. Chen, *Phys. Rev. Lett.* **2005**, *94*, 146402-1-4.
- [40] T. Kroll, M. Knupfer, J. Geck, C. Hess, T. Schwieger, G. Krabbes, C. Sekar, D. R. Batchelor, H. Berger, B. Büchner, *Phys. Rev. B: Condens. Matter Mater. Phys.* **2006**, *74*, 1-6.
- [41] H. Hirsh, Y. Li, J.-H. Cheng, R. Shimizu, M. Zhang, E. Zhao, Y. S. Meng, *J. Electrochem. Soc.* **2021**, *168*, 040539.
- [42] K. Luo, M. R. Roberts, R. Hao, N. Guerrini, D. M. Pickup, Y. S. Liu, K. Edström, J. Guo, A. V. Chadwick, L. C. Duda, P. G. Bruce, *Nat. Chem.* **2016**, *8*, 684-691.
- [43] K. Luo, M. R. Roberts, N. Guerrini, N. Tapia-Ruiz, R. Hao, F. Massel, D. M. Pickup, S. Ramos, Y. S. Liu, J. Guo, A. V. Chadwick, L. C. Duda, P. G. Bruce, *J. Am. Chem. Soc.* **2016**, *138*, 11211-11218.
- [44] M. Okubo, A. Yamada, *ACS Appl. Mater. Interfaces* **2017**, *9*, 36463-36472.
- [45] A. A. Coelho, *J. Appl. Crystallogr.* **2018**, *51*, 210-218.
- [46] B. Ravel, M. Newville, *J. Synchrotron Radiat.* **2005**, *12*, 537-541.
- [47] B. Ravel, M. Newville, *Phys. Scr.* **2005**, *T115*, 1007-1010.
- [48] H. Ohashi, E. Ishiguro, Y. Tamenori, H. Kishimoto, M. Tanaka, M. Irie, T. Tanaka, T. Ishikawa, *Nucl. Instruments and Methods Phys. Res. A* **2001**, *467-468*, 529-532.

Manuscript received: March 3, 2022

Revised manuscript received: March 29, 2022

Accepted manuscript online: April 20, 2022